SAR Retracking in the Arctic

Development of a year round Arctic SAR retracker system

Ann-Theres Schulz

Master of Science Thesis

Delft University of Technology

Astrodynamics and Space Missions

SAR Retracking in the Arctic

Development of a year round Arctic SAR retracker system

by

Ann-Theres Schulz

To obtain the degree of Master of Science
in Spaceflight at Delft University of Technology,
to be defended publicly on 15 April 2016 at 9.00.

Student number:	4124251	
Thesis committee:	Ir. M.C. Naeije	TU Delft, supervisor
	Prof.dr.ir. P.N.A.M. Visser	TU Delft
	Dr.ir. E.J.O. Schrama	TU Delft
	Dr.ir. D.C. Slobbe	TU Delft

An electronic version of this thesis is available at http://repository.tudelft.nl/.

Cover Picture: Artist's impression of CryoSat-2. Image Courtesy: European Space Agency.

Abstract

Developments in satellite altimetry over the past years lead to a high resolution altimeter: Synthetic Aperture Radar (SAR). The major improvement of SAR over pulse-limited altimeters is the increased along-track resolution. Since CryoSat-2 is the first satellite to carry a SAR altimeter it serves as a stepping stone to improve the performance of SAR. Given its polar orbit, CryoSat-2 provides frequent high resolution measurements of the Arctic region over changing terrain (e.g. ice, water and sea ice).

Due to the high seasonality in the Arctic, it is of essence that the quality of SAR measurements is not decreased with varying topography. Therefore, the purpose of this research is to improve SAR waveform retracking in the Arctic region by analyzing different retrackers on their performance in varying (Arctic) conditions and combine the positive behavior into one retracker system.

The research is separated into three parts, first the SAR waveforms are classified, secondly the retrackers' performance is evaluated and finally, the combined retracker system is discussed.

The waveforms are classified according to open ocean, sea ice and leads based on their statistical behavior and the number of major peaks. Leads are waveforms caused by fractures in the sea ice resulting in water presence in the ridges. Throughout 2011, the number of waveforms per terrain shows a high seasonality with a large amount of sea ice in January to April, high leads percentage in May to June and finally, a large number of ocean observations in September to October.

Based on the accuracy and precision performance, four retrackers are evaluated in order to determine a retracker system: the empirical primary peak Center of Gravity (COG), the primary peak threshold and the ESA retracker as well as the physical SAMOSA3 retracker. Empirical retrackers determine the retracking point depending on the waveform statistics, while physical retrackers take the surface properties into account.

The accuracy is evaluated using coastal tide gauges and Envisat crossovers for ocean waveforms only, as this data is not representative for leads or sea ice. For the majority of the months SAMOSA3 has the highest accuracy for ocean waveforms as its physical full analytic approach provides a good fit for the predictable ocean waveforms. The primary peak retrackers have the best precision performance for irregular waveforms like sea ice and leads, as they are less sensitive to noise since only the maximum peak is analyzed.

The year round retracker system includes the most accurate retracker for ocean waveforms per month and the best precision retracker for sea ice and leads. When combining different retrackers the bias caused by different algorithms needs to be removed. A mean bias strategy is implemented that computes the mean offset between two retrackers per track over open ocean and the offset is then applied to the other waveform classes. A bias removal approach based on significant wave height dependency is also applied using least squares to compute the offset per waveform class per track. Furthermore, two hybrid models of these strategies are implemented. The first hybrid model uses the significant wave height model for ocean observations and the mean bias method for leads and sea ice to remove the offset. Within the second hybrid model, the ocean and leads bias is removed by the significant wave height approach, while the offset in the sea ice class is mitigated with the mean bias method.

The retracker system with the primary peak center of gravity as a base retracker and a mean bias removal approach performed best as it has a precision improvement of 47.1% with respect to retracking all waveform classes with the primary peak COG while including the largest data set for precision and accuracy determination.

Table of Contents

List of Figures

List of Tables

Glossary

List of Acronyms

CNSA	China National Space Administration
COG	Center of Gravity
DORIS	Doppler Orbitography and Radio positioning Integrated by Satellite
DTU	Denmarks Tekniske Universitet
ECMWF	European Centre for Medium-Range Weather Forecasts
ESA	European Space Agency
GIA	Glacial Isostatic Adjustment
GIM	Global Ionospheric Map
GPOD	Grid Processing On Demand
GPS	Global Positioning System
LRM	Low-Resolution Mode
NOAA	National Oceanic and Atmospheric Administration
NOC	National Oceanography Centre
POD	Precise Orbit Determination
PRF	Pulse Repetition Frequency
PSMSL	Permanent Service for Mean Sea Level
RADS	Radar Altimeter Database System
SAMOSA	SARL Altimetry MOde Studies and Applications
SAR	Synthetic Aperture Radar

SARIn	Synthetic Aperture Radar Interferometer
SCOOP	SAR Altimetry Coastal & Open Ocean Performance
SIRAL	Synthetic Aperture Interferometric Radar Altimeter
SLR	Satellite Laser Ranging
SWH	Significant Wave Height

List of Symbols

Greek Symbols

Δ	Difference	$[-]$
γ	Antenna pointing angle	[deg]
λ	Wavelength	[m]
ϕ	Latitude	[deg]
ρ	Density	$[\mathrm{kg/m^3}]$
σ	Backscatter coefficient	$[-]$
φ	Phase shift	[deg]
$\vec{p}$	Vector to a point on the surface with respect to nadir	$[-]$

Latin Symbols

A	Amplitude	[W]
BP	Burst period	[s]
C	Retracking point	[bins]
c	Speed of light	[m/s]
f	Frequency	[Hz]
G	Gaussian fit	$[-]$
H	Altitude with respect to the reference ellipsoid	[m]
h	Sea surface height	[m]
k	Antenna illumination property	$[-]$
L	Columnar liquid water	[m]
MSS	Mean Sea Surface	[m]
N	Number of echoes	$[-]$
PP	Pulse Peakiness	$[-]$
PRF	Pulse Repetition Frequency	[Hz]
P	Power	[W]
q	Topographic distribution	[W]
RIR	Range Impulse Response	$[-]$
R	Range	[m]

SLA	Sea Level Anomaly	[m]
SSD	Stack Standard Deviation	[−]
TL	Threshold Level	[−]
T	Temperature	[K]
t	Time	[s]
u	Wind speed	[m/s]
V	Velocity	[m/s]
W	Width	[−]

Subscripts

ANN	Annual
Ant	Antenna
a	Atmospheric pressure loading
cor	Corrected
Dop	Doppler
dry	Dry troposphere
d	Dynamic
E	Earth
FS	Flat surface
g	Geoid
ib	Inverse Barometer
$iono$	Ionosphere
MDT	Mean Dynamic Topography
min	Minimum
MSS	Mean Sea Surface
obs	Observed
orb	Orbit
pp_cog	Retracking point of the center of gravity primary peak retracker
pp_thres	Retracking point of the threshold primary peak retracker
P	Pulses
r	Received
ssb	Sea state bias
$thres$	Threshold
tr	Transmitted
t	Tide
wet	Wet troposphere
wf	Waveform

Preface

Besides marking the end of my studies, this thesis also means that I finished my research on how the sea level measurements in the Arctic region can be improved. The Arctic region provides an insight into the development and changes of the Earth's climate. Looking at the Arctic, provides us a with a look into the future for the rest of the planet. In a time where sea ice and ice sheet melting are old news, the effects of this need to be examined in more detail. The development of a year round retracker helps with this aim since it improves sea level measurement performance.

The MSc topic arose in collaboration with DTU Space that is an expert in the field of polar altimetry. DTU Space has developed and compared several retrackers specifically for SAR conditions and therefore provided the stepping stone for this research.

I would like to express my gratitude to Marc Naeije for his guidance and support throughout the last months. Thank you for making our weekly meetings entertaining while always keeping the goal of my research in mind. My gratitude extends further to the committee member Prof.dr.ir. Visser, Dr.ir. Schrama and Dr.ir. Slobbe. Further, I would like to thank Ole B. Andersen and Lars Stenseng (DTU Space) for never getting tired of answering my questions and providing me with feedback. Maulik Jain (DTU Space) did not only provided me with his software for the primary peak retrackers, but also guided me into the topic of polar altimetry. I am thankful to Salvatore Dinardo who took the time to look at my results of SARvatore and to Jerome Bouffard (ESA) for arranging access to CryoSat level 2 data, after the server was taken offline.

The never ending support and patience of my parents always kept me grounded. I am deeply grateful for your trust that I will pave my way and all the opportunities that you provided me with. Finally, I would like to thank all my friends that became such an important part of my life over the past years and who invariably made my Delft experience so special.

Delft, University of Technology — Ann-Theres Schulz

Chapter 1

Introduction

The field of satellite altimetry has done a big leap forward throughout the past years. Up to 2010, satellite altimeters were based on a pulse-limited method which resulted in a big footprint. However, the focus of altimetry was turned by the development of Synthetic Aperture Radar (SAR) and its integration into the first satellite - CryoSat-2. Compared to conventional altimeters, SAR provides high resolution measurements that have a significantly smaller footprint as compared to pulse-limited altimeters [1]. Therefore, CryoSat-2 serves as a stepping stone for future missions and developments. Another distinct feature of CryoSat-2 besides the SAR altimeter, is its polar orbit. With the polar orbit, CryoSat-2 provides frequent, high resolution observations of Arctic and Antarctic regions [2].

While the SAR technology has been assessed using airborne altimeters on small areas [3], the impact of using a SAR altimeter in the Arctic region over different terrains needs to be explored in more detail. The Arctic region shows strong seasonal behavior with a significant change in ice and sea ice presence over the year. As SAR measures over different surface types (e.g. water and sea ice), the performance of the altimeter is affected and a potential performance decrease needs to be prevented [4].

By developing an Arctic retracking system that is able to cope with different terrains and significant seasonal behavior, the performance of sea surface height, ice presence and ice sheet thickness measurements can be increased. Therefore, the necessity of an improved retracking determination emerges.

The purpose of this research is to develop an all year round retracking system for the Arctic region, more specifically:

> *The objective of this research is to improve SAR waveform retracking in the Arctic region by analyzing different retrackers on their performance in varying (Arctic) conditions and combine the positive behavior into one retracker system.*

In order to achieve this purpose the research is split into three parts: waveform classification, retracker performance analysis and the development of a year round retracker system. During the waveform classification, the effect of different terrains on SAR waveforms will be investigated and what parameters can be used to express their characteristics.

The second part of the research focuses on the evaluation of retracker performance. For this, performance criteria are selected and applied to the retrackers for each waveform class that was defined in the first segment. Furthermore, the seasonal performance of retrackers is assessed here.

In the final section of this research, the challenges of developing a retracking system for the Arctic region are analyzed. When combining different retrackers into one comprehensive retracking system, a relative offset between the different retrackers occurs. To remove this offset, appropriate bias removal strategies are used in order to have a coherent retracker system for the Arctic region.

In order to address the research purpose, first, the mission objective of CryoSat-2 and its altimeter operational modes are discussed in Chapter 2. An introduction into radar altimetry and the required signal correction is provided in Chapter 3. Here, the working principle of the SAR altimeter is explained and the data used in this research is briefly described. Next, the first research segment is addressed. In Chapter 4, the waveform classification and the used parameters are described. Furthermore, the seasonal behavior of the Kara Sea in the Arctic region is assessed.

The design of the selected retrackers is described in Chapter 5, followed by an analysis of their performance with respect to precision and accuracy in Chapter 6. The final segment of the research is presented in Chapter 7 and discusses different bias removal strategies used for the selected year round Arctic retracker system. The performance of the bias removal strategies are assessed based on the retracker system performance using each strategy. Finally, conclusions are drawn and recommendations are presented in Chapter 8.

Chapter 2

CryoSat-2

In the following, first the mission objective and characteristics of CryoSat-2 is discussed, then an introduction in the different operational modes of the altimeter is given.

2-1 Mission

CryoSat-2 marks a turning point in the history of altimetry as it is the first satellite to have an on-board Synthetic Aperture Radar (SAR) altimeter. With this high-resolution instrument, CryoSat-2 provides more detailed information about sea-level and ice presence compared to previous altimetry missions.

Mission Parameters

CryoSat-2 was launched in April 2010 with a mission objective to observe the changes in land and sea ice [5]. With an inclination of 92° and an altitude of 717 km, CryoSat-2 is able to reach latitudes up to 88° and therefore, able to perform measurements in the Arctic regions [6]. Furthermore, CryoSat-2 performs geographically complete observations of land and sea ice, due to its large repeat cycle of 369 days with a sub-cycle of 30 days [6].

Given the mission objective, it is essential to have both, a precise orbit and position determination of the satellite. CryoSat's Precise Orbit Determination (POD) is based on three star trackers which are able to take a maximum of five pictures per second [6]. Concerning an accurate position determination, two instruments are used: DORIS and laser retro-reflectors. Doppler Orbitography and Radio positioning Integrated by Satellite (DORIS) consists of one-way measurements that computes the Doppler shift of a signal leading to the position determination [7]. In case of CryoSat-2, a receiver is placed on-board of the satellite, while the transmitters are ground-based. The laser retro-reflector is based on the concept of Satellite Laser Ranging (SLR). Here, a laser pulse is sent towards the satellite which then reflects it back to the exact location where the pulse originated. A network of SLR observation stations are used to transmit and receive laser pulses. The two-way travel time of the laser pulse then provides information about the satellite position for CryoSat-2 [7].

2-2 Altimeter Operational Modes

Synthetic Aperture Interferometric Radar Altimeter (SIRAL) is the on-board altimeter on CryoSat-2 that transmits pulses in Ku-band (13.575 GHz) [6]. SIRAL can be operated in three modes: Low-Resolution Mode (LRM), Synthetic Aperture Radar (SAR) and Synthetic Aperture Radar Interferometer (SARIn).

Generally, LRM is used over oceans and ice sheet interiors, while SAR measures over sea ice and SARIn is applied around ice sheet margins and over mountain glaciers [6]. It should be noted, that while LRM transmits pulses continuously at a frequency of 1970 Hz, SAR transmits pulses in bursts at a frequency of 17.8 kHz. The significantly higher frequency of the SAR mode consequently leads to a shorter time interval resulting in correlated echoes [6].

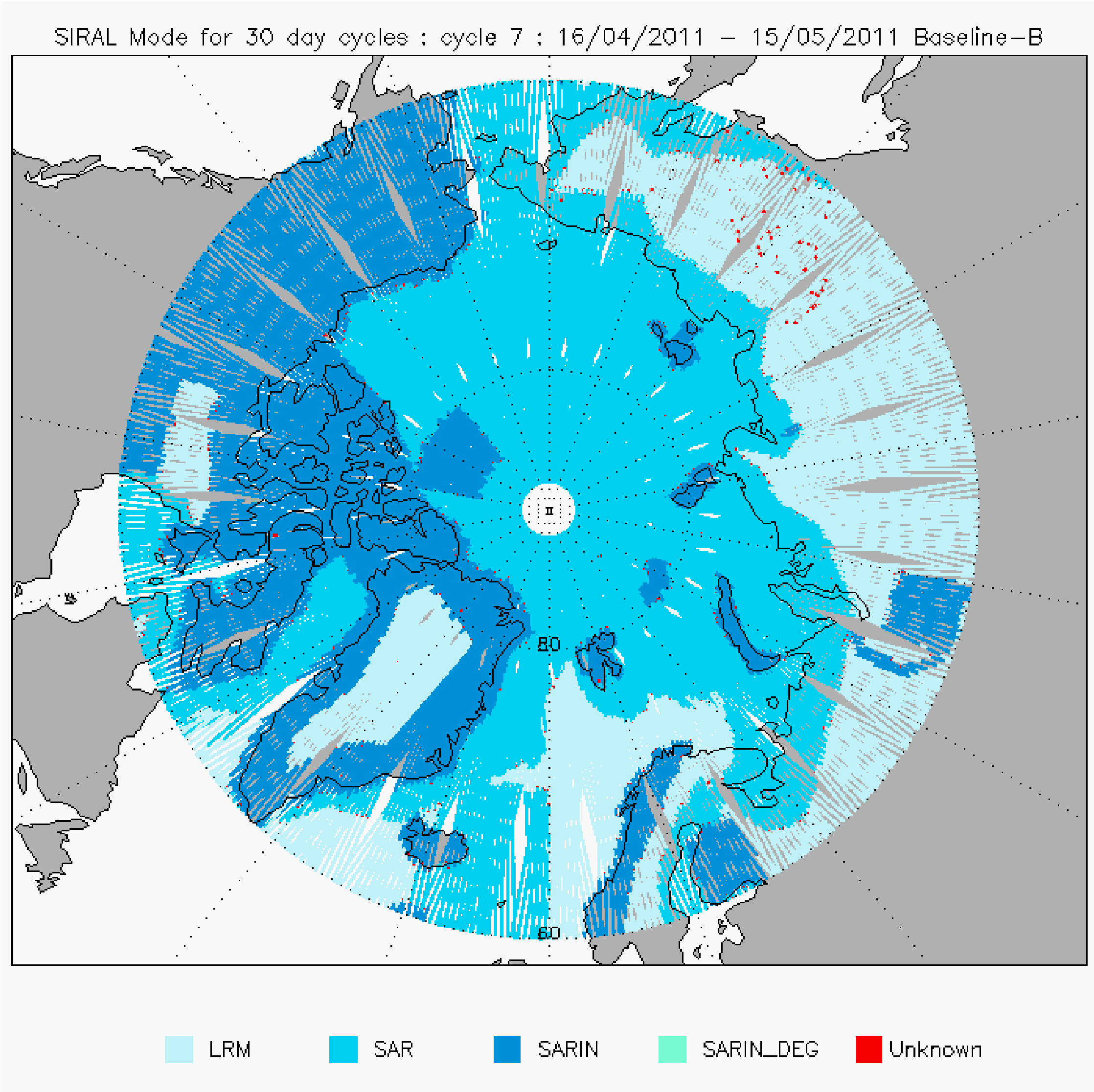

Figure 2-1: CryoSat-2 mode mask for the Arctic from 16/04/2011 to 15/05/2011 [8]. SARIN$_{DEG}$ indicates degraded SARIn mode.

Figure 2-1 shows an example of the CryoSat-2 geographical mask for the Arctic region for a one month time frame (16/04/2011 - 15/05/2011). It can be observed that the Arctic ocean and part of the coastal region are predominantly observed in SAR mode, while a significant part of the Arctic coastal region is also determined by SARIn. Due to large coverage of SAR in the Arctic by CryoSat-2 and future missions, the need to improve retracking in the Arctic becomes apparent. To account for the constantly changing ice regions, the geographical mode mask of SIRAL is updated every two weeks.

Chapter 3

Radar Altimetry

Satellite altimetry provides a frequent and global observations of the Earth surface. In this chapter the principle of radar altimetry and the required corrections to compensate delays of the electromagnetic signal are discussed. Based on the general principle of altimetry, the working principle of Synthetic Aperture Radar (SAR) altimetry is reviewed. Finally, the acquisition and processing of the data used in this research is described.

3-1 Principle of Radar Altimetry

The basic principle of radar altimetry is that a radar pulse in the microwave range is transmitted nadir by a satellite and then the reflected echo is received by the satellite from the surface.

Based on the properties of returned echo, the range, thus the distance between satellite and sea surface, can be computed. Further, information about the topography can be retrieved.

Figure 3-1 shows the geometry of radar altimetry, it is visible that the pulse is affected by atmospheric refraction and biases [10]. More information about corrections that are applied is given in Section 3-2. The range, R, of the satellite can be computed using the two-way travel time as shown in Eq. (3-1) [11],

$$R = c\frac{t_r - t_{tr}}{2} \tag{3-1}$$

where c represents the speed of light. The transmitted time, t_{tr} and received time, t_r are measured by satellite.

Consequently, the corrected range can be expressed by Eq. (3-2) [12]. The range corrections that are applied are the dry troposphere correction, Δh_{dry}, the wet troposphere correction, Δh_{wet}, the ionosphere correction, Δh_{iono}, and the sea-state bias, Δh_{ssb}. Based on the corrected range, the sea surface height, h, relative to the reference ellipsoid is determined using Eq. (3-3). Here, H, represents the satellite altitude with respect to the reference ellipsoid.

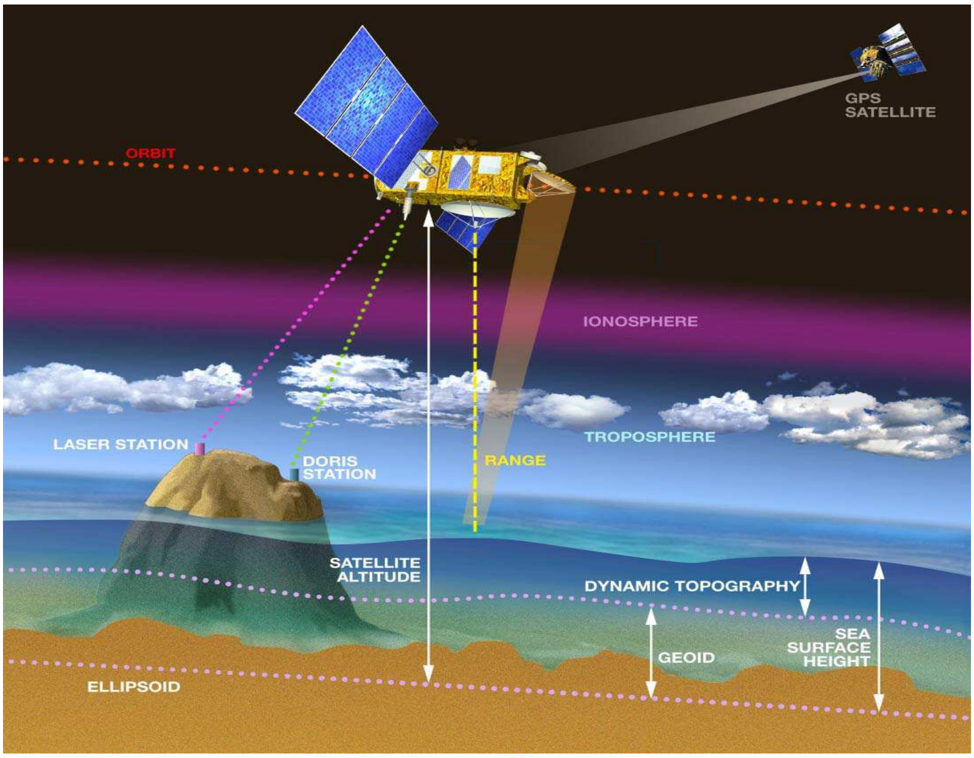

Figure 3-1: The geometry of altimetry observations [9].

$$R_{cor} = R_{obs} - \Delta h_{dry} - \Delta h_{wet} - \Delta h_{iono} - \Delta h_{ssb} \tag{3-2}$$

$$h = H - R_{cor} \tag{3-3}$$

Figure 3-2 shows the geophysical corrections that apply to the sea surface height such as geoid height h_g, tidal height h_t, atmospheric pressure loading h_a and dynamic ocean topography h_d. The geophysical corrections will be explained later in this chapter. Applying the geophysical correction, the sea surface height can be expressed by Eq. (3-4).

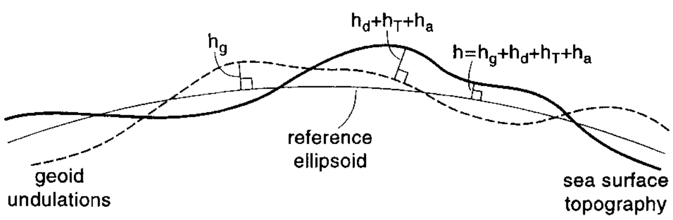

Figure 3-2: The geophysical corrections that are applied to the sea surface measurement: Geoid height, tidal height, atmospheric pressure loading and dynamic effects of geostrophic ocean currents [10].

$$h = h_d + h_a + h_g + h_t \tag{3-4}$$

For oceanographic purposes, the study of the dynamic sea surface height is of primary importance. The dynamic height can be expressed as a function of the range and geophysical corrections as shown in Eq. (3-5) [12].

$$h_d = H - R_{obs} - \Delta h_{dry} - \Delta h_{wet} - \Delta h_{iono} - \Delta h_{ssb} - h_t - h_a - h_g \tag{3-5}$$

Before the individual corrections are explained, an error budget is given in Figure 3-3. It shows an overview of the errors in the individual corrections for different altimeter missions. A clear improvement can be seen over time. The largest error remains in the orbit determination, however, also the range corrections can have an error of up to a few centimeter. The error in the corrections vary spatially as will become apparent in the following section. It should be noted that the error budget shown here is based on data up to 2007. However, there is the constant endeavor to further reduce the error in the corrections. The total orbit and range error budget for CryoSat-2 SAR expressed as the total root sum square (RSS) is determined to be 11.6 cm [13].

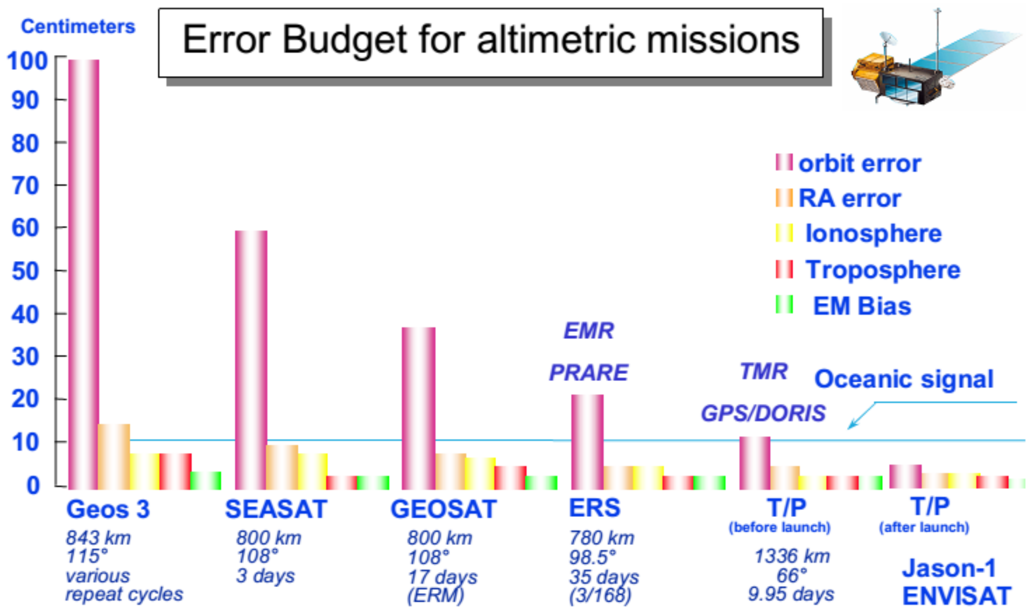

Figure 3-3: Error budget for past altimeter missions [9].

3-2 Geophysical and Range Corrections

In the previous section it was shown that the measured range by the altimeter is not only exposed to atmospheric refraction but also geophysical properties. The mean value of the geophysical and range time-variable corrections is given in Table 3-1. In the following, the principle of the corrections and the models used in this research are shortly elaborated.

Table 3-1: Mean and the standard deviation of the time-variable geophysical and range corrections. The mean is given as a negative value as it needs to be subtracted from the sea surface height. Furthermore, the standard deviation, thus the variation of the correction values, is given for deep ocean scenario. The values are based on 6 years of altimeter data of Jason-1 [12].

	Mean [cm]	**Standard deviation of time-variable corrections for deep ocean [cm]**
Dry troposphere	-231	0 - 2
Wet troposphere	-16	5 - 6
Ionosphere	-8	2 - 5
Sea-state bias	-5	1 - 4
Tides	$\sim$ 0 - 2	0 - 80
Dynamic atmosphere	$\sim$ 0 - 2	5 - 15

Dry Troposphere

The dry troposphere correction is the largest contributor to the refraction experienced by the transmitted and received signal. The interaction of dry gas components in the atmosphere with the signal leads to this refraction [10].

In order to correct for this refraction, the European Centre for Medium-Range Weather Forecasts (ECMWF) model is used that computes the sea level pressure. Based on the sea level pressure, the dry troposphere correction is then determined. The precision of this model in the Arctic region is varying between 2.5 - 3.75 cm [12].

Wet Troposphere

The wet troposphere refraction is caused by water vapor and liquid water droplets [10]. At high latitudes only small wet troposphere refraction occurs. Since CryoSat-2 does not have an on-board radiometer, the wet troposphere correction is obtained by ECMWF.

Ionosphere

As the electromagnetic wave propagates through the ionosphere it interacts with free electrons and ions resulting in the ionosphere delay [10]. The ionosphere starts at an altitude of 80 km [14]. Towards higher latitudes, the ionosphere correction as well its variability decreases [12]. The ionosphere correction is corrected using the Global Ionospheric Map (GIM) which is computed using Global Positioning System (GPS) satellites. These satellite determine the total electron content globally in a 5-15 minutes time interval [15].

Sea-State Bias

Sea-state bias (SSB) is caused by a combination of effects: the electromagnetic (EM) bias, the skewness bias and an instrument retracker bias.

The electromagnetic bias is caused by the different backscatter from troughs and crests. Due to the larger curvature of troughs in a non-Gaussian sea surface, a higher backscatter power is produced compared to the crests which have a smaller curvature and therefore a lower backscatter power [10].

Since the altimeter measures the sea surface using the median scattering instead of the desired mean scattering, the skewness bias occurs [12].

The last element of the sea-state bias is the instrument error caused by the retracker. The retracker produces the waveform by analyzing the received power. Based on the waveform, the Significant Wave Height (SWH) can be determined which is equal to the height of the 1/3 highest waves [12].

No sea-state bias is applied to the data, as no appropriate correction model is available for SAR at the time of this research. However, there are projects like SAR Altimetry Coastal & Open Ocean Performance (SCOOP) that aim to develop a SAR SSB model [16].

Marine Geoid

The marine geoid represents an equipotential surface that would coincide with the mean sea surface, if the oceans are at rest [17]. The spatial deviation throughout the Earth in the marine geoid are caused by inhomogeneities in the interior density of the Earth [12]. The marine geoid undulations are the largest geophysical correction applied to the range equation.

In order to correct for the marine geoid, the mean sea surface (MSS) will be removed from the data. The mean sea surface is the sum of the marine geoid and the mean dynamic topography [12]. It is applied through DTU13 resulting in a more detailed correction model.

Tides

The total tidal height consists of four main components as described by (3-6) [12]. The two biggest contributors that influence the ocean tide, h_{ocean}, are the Earth rotation with respect to the sun and to the moon. The loading tide, h_{load}, indicates the sea floor displacement due to additional water masses [12]. Both, the ocean tide and the loading tide are modeled by FES2004. It is provided as 1 Hz observations in the ESA Level 1b and Level 2 data [6] and as 20 Hz data in the SAMOSA processing by SARvatore [18].

$$\Delta h_t = \Delta h_{ocean} + \Delta h_{load} + \Delta h_{solid\_Earth} + \Delta h_{pole} \tag{3-6}$$

The solid Earth tide, h_{solid_Earth}, is caused by the gravitational forces with other bodies, which leads to a vertical displacement proportional to the tidal potential [10]. This component is determined using the Cartwright model as discussed in [19].

The last component, the pole tide, h_{pole}, is corrected using historical pole location data. It represents the ocean's behavior to the deviation in equilibrium solid Earth and ocean caused by the change in the rotation axis of the Earth [7].

Atmospheric Pressure Loading

The atmospheric pressure loading compensates for high or low pressure occurrences over the sea surface. Two different methods are used to compensate for this geophysical offset. First of all, the inverse barometric correction is calculated as described in [12] and used to adjust for the atmospheric pressure variations over sea ice and leads [6].

Secondly, the dynamic atmospheric correction is applied to the open ocean by using the MOG2D (two dimensional gravity wave model) to compensate for atmospheric pressure and winds [20].

3-3 Synthetic Aperture Radar

Synthetic Aperture Radar is also known as an along-track directional beam-limited altimeter that observes a certain cell with multiple narrow antenna beams to achieve a high along-track resolution [21]. The foundation of SAR which is also called a Doppler/delay radar altimeter is described in detail in [1].

Geometry

The basic principle behind SAR is that one cell on the ground will be illuminated over a period of time and the returned echoes can be used to form one waveform of the observed cell [22]. The different frequency shifts in case of off-nadir observations, are compensated using Doppler shifts. Figure 3-4 shows the observation geometry of SAR on the left hand side and the footprint on the right hand side.

Due to the use of multiple beams to form the observation of a cell, SAR uses significantly more radiated energy to determine the waveform compared to beam-limited altimeters [1]. To process each Doppler cell as shown in the right of Figure 3-4, coherent observations are used over time. While the pulse-limited altimeter can be processed with one independent variable, SAR has two independent variables: along-track (function of range) and cross-track positions (function of time delay). Figure 3-4 shows clearly that the along-track distance remains constant over time per Doppler bin, while the cross-track distance decreases as a function of time.

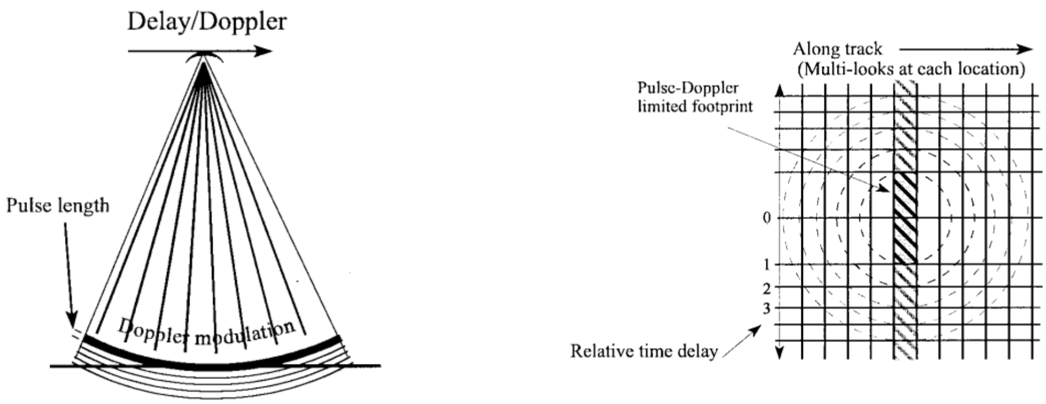

Figure 3-4: The geometry of SAR. *Left:* The along-track beams emitted by the altimeter reaching the surface. *Right:* The footprint of SAR [1].

Also the cross-track ambiguity can be observed, since every received scatter could originate from either side of the nadir point as it has a given time delay associated with the scatter [1].

Similar to conventional altimeter, the average rough surface response, $P_I(t)$, can be expressed by the convolution in Eq. (3-7), where P_{FS} is the flat surface response, $q(t)$ is the topographic distribution, $P(t)$ is the impulse response and P_{FS0} is the idealized flat surface response [1], [23].

$$P_I(t) = P_{FS}(t) * q(t) \tag{3-7}$$

with

$$p_{FS} = P(t) * P_{FS0}(t) \tag{3-8}$$

There is a distinct difference between the two flat surface responses used above. While P_{FS0} is the idealized flat surface, P_{FS}, takes into account the limitations of the measurement geometry [1].

Burst Method

Contrary to pulse limited altimeters, SAR sends pulses in bursts at a significantly higher frequency. For conventional altimetry, the Walsh bound computes the maximum Pulse Repetition Frequency (PRF) that will lead to uncorrelated signals [24]. Based on this relationship, the Walsh bound can be expanded to determine the lower burst period limit for SAR. The minimum burst time, BP_{min}, is inversely proportional to PRF as indicated by Eq. (3-9). Here, N_P is the number of pulses per bursts. With a higher PRF, the burst period decreases.

$$BP_{min} = \frac{N_P}{PRF} \tag{3-9}$$

A small along-track distance of the Doppler cell is required in order to achieve a high number of useful observations. Assuming that the number of pulses per burst stay the same, the number of useful observation decreases, if the PRF increases.

Generally, there are three options on how SAR measurements can be conducted, either using an open-burst method, a closed-burst method or a continuous PRF. Figure 3-5 shows the procedure behind the open and closed burst method.

As can be seen in the top panel of Figure 3-5, the closed burst method transmits pulses in bursts. The reflected echoes are then received as a group. In this case, the burst period is constant and consists of the length of transmitted and received burst.

The approach of closed burst SAR is used on CryoSat. However, CryoSat makes use of only 1/3 of its available looks, since its burst period is about three times larger than the minimum burst period computed by the Walsh bound [21].

The bottom panel of Figure 3-5 shows the open burst method. In contrast to the closed approach, the open burst method receives the reflected pulses between transmitted pulses [21]. The burst period is variable to account for the varying altitude that the satellite encounters. A variation of up to 5 % in burst period is sufficient to take this change into consideration [1]. In case of an open burst approach, the pulse length is smaller than half of the constant PRF.

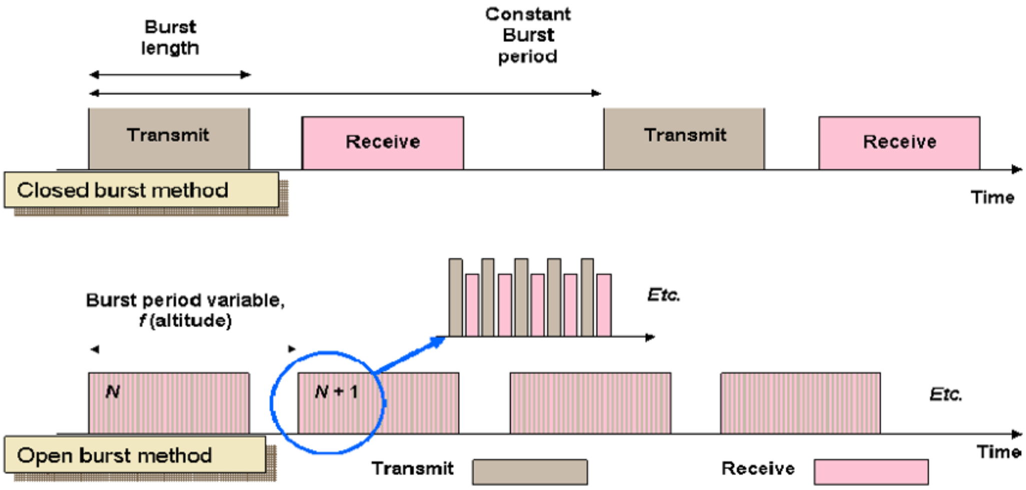

Figure 3-5: *Top panel:* The closed burst method is shown as used in CryoSat-2. *Bottom panel:* The open burst method with the individual transmitted pulses in grey and the received ones in pink [21].

In case of a high PRF, the challenge arises to transmit long pulses due to the relatively small transmission time, therefore, smaller PRFs are used in the open burst approach to have the required reception time available between transmitting two pulses.

Jason-CS (Continuity of Service), also known as Sentinel-6, will have an on-board radar altimeter that uses the open burst method in SAR mode [25].

The third method of a working SAR is to have a continuous PRF, similarly to conventional altimetry. Here, the PRF would be a function of the spacecraft altitude and therefore, would vary throughout the mission. While this system architecture would significantly increase the number of independent looks available, also a higher system complexity is required [21].

Precision

Based on the received echo, waveforms can be determined which will provide main statistical parameters of the surface such as significant wave height (SWH), sea surface height (SSH) and wind speed (based on the backscatter).

Comparing the SAR instrument to conventional altimeters as shown in Figure 3-6, it can be observed that a significant reduction in standard deviation occurs for all SWH. This leads to an improvement of factor two in the precision measurements and of factor 10 of the signal to noise ratio [26].

Due its smaller along-track footprint size, SAR is less influenced by land contamination compared to conventional altimetry. Consequently, waveforms in coastal area can be created with less land influence [27].

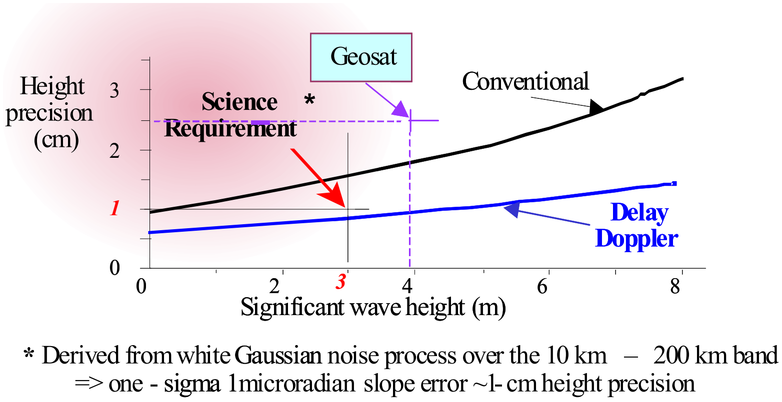

Figure 3-6: SAR precision (blue) in cm shown as a function of significant wave height. As a reference, the precision of pulse limited altimeters (black) is indicated [26].

3-4 Data Acquisition

In this research four different retrackers are analyzed and compared based on their seasonal performance as will be discussed in the following chapters. For this purpose different data sources are used to obtain the relevant retracker data as shown in Table 3-2. The primary peak retrackers use ESA's level 1b baseline B data and the CryoSat-2 retracker is based on baseline B level 2 data retrieved from ESA's ftp server.

To the level 1b data calibration corrections are applied and geophysical and range corrections are provided. CryoSat-2 level 2 data is fully corrected for time, geo-location and surface height [6]. The level 1b data is based on 20 Hz observations, however, the corrections provided by ESA are given in 1 Hz intervals. Therefore, the corrections are spatially interpolated in order to provide 20 Hz corrections. These corrections match well with the corrections obtained by the SARvatore software [18].

Furthermore, a range bias and a time tag bias was observed in Baseline B that was corrected in SARvatore [28]. Therefore, both level 1b and level 2 were corrected for a 67.3 cm range bias and a 0.5195 μs time tag bias.

The steps that are undertaken in order to determine the sea level anomaly starting with the level 1b Baseline B data is shown in Figure 3-7.

The data handling of tide gauges and Envisat observations will be discussed in more detail in Section 6-2.

Table 3-2: The data and its sources used in this research.

	Source
CryoSat-2 SAR level 1b	ESA
CryoSat-2 SAR level 2	ESA
SAMOSA	SARvatore - GPOD
Tide gauge observations	PSMSL
Envisat observations	RADS

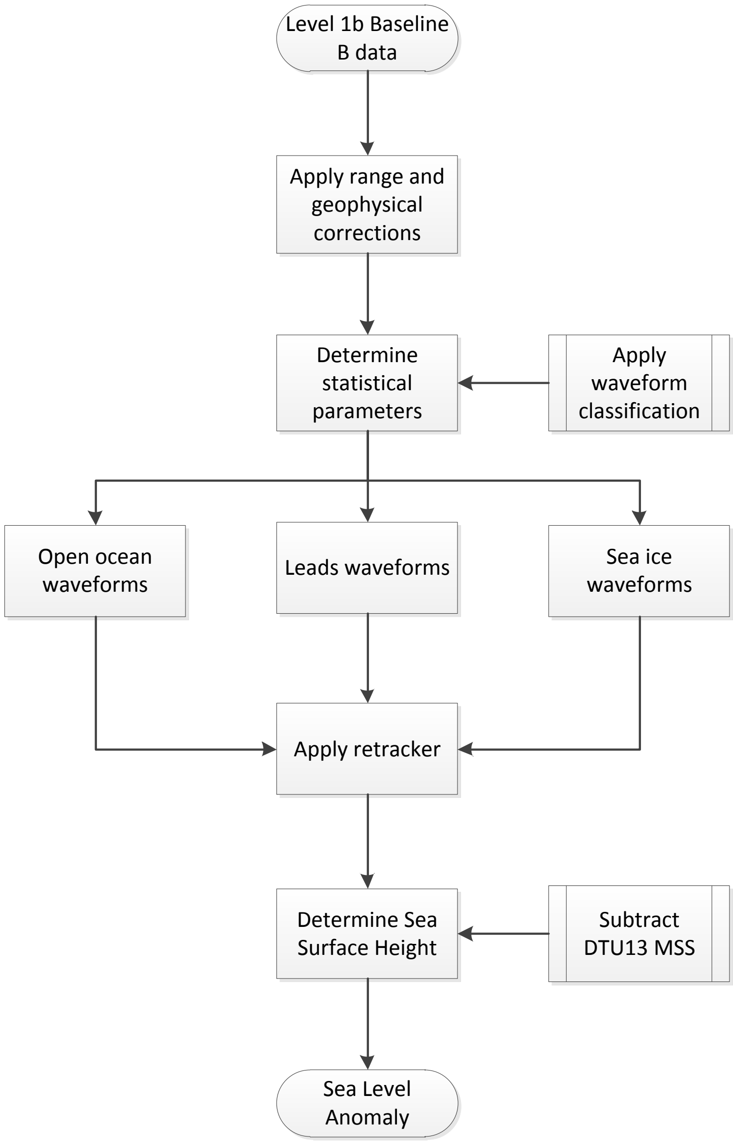

Figure 3-7: Flowchart for the data processing of ESA level 1b Baseline B measurements.

Chapter 4

Waveform Classification

Waveforms provide valuable information about the observed surface terrain and can be classified accordingly. Three different surface types are implemented in this research: ocean, leads and sea ice. An introduction into waveforms and the classification parameters implemented in this research is provided in Section 4-1. Afterwards, characteristics and waveform shapes for ocean, leads and sea ice are presented. Section 4-5 discusses the seasonality in the Arctic for the selected test region.

4-1 Waveform

When observing different terrains using an altimeter, the behavior of the returned power varies. The shape of the returned power over time is called a waveform [5] and provides knowledge about the sea surface characteristics.

Given its high seasonality, the polar region contains multiple surface types that result in different waveforms: open ocean, coastal regions, land and sea ice and leads [29]. Lead waveforms are caused by the appearance of water in sea ice fractures and will be addressed in more detail in Section 4-3, while sea ice describes a surface type that contains scattered ice floes over open water [30].

As previously discussed, the returned power by SAR altimetry is a function of two independent variables, the cross-track (function of time delay) and along-track positions (function of range). Figure 4-1 shows the resulting waveform over a flat surface that has an impulse like shape. The waveform shape is a consequence of the 2 dimensional processing of the data [1]. A large number of equivalent looks at a given position are determined by accumulating range values at each Doppler bin. The footprint of SAR decreases as a the time delay increases, while the along-track distance remains constant as shown in Figure 3-4. Consequently, the majority of the return power is received directly nadir with small time delay. With an increase in time delay less returned power is received, given the smaller SAR footprint, leading to a waveform with an impulse like shape.

Based on the received power, different waveform classes can be established in order to differentiate between surface types. A number of waveform classes for pulse-limited altimetry are shown in Figure 4-2. Despite the different waveform behavior for SAR altimetry with respect to conventional

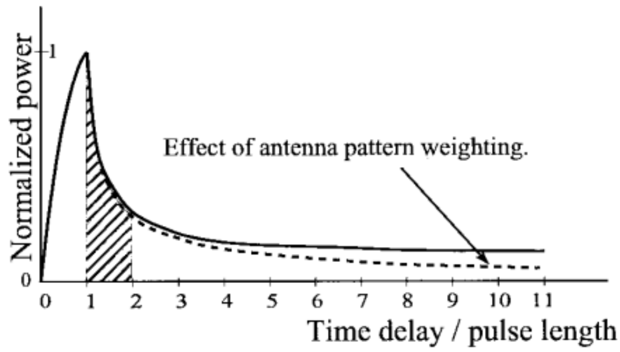

Figure 4-1: The SAR waveform has a steep peak followed by a slowly decaying trailing edge [1].

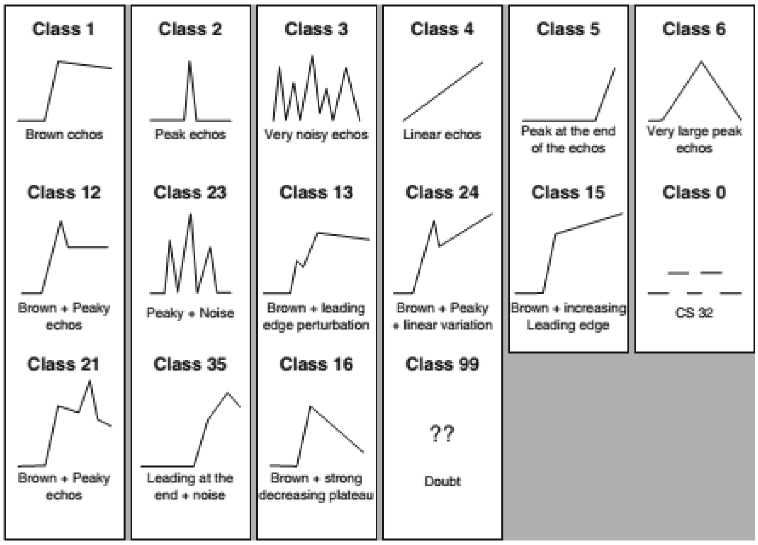

Figure 4-2: Different waveform classes based on pulse limited altimetry [31].

altimetry, it becomes apparent that waveform classes need to be well defined to prevent falsely classifying a SAR waveform.

The sea surface height is computed using either empirical or physical retrackers that are discussed in Chapter 5. However, retrackers that are designed for open ocean purposes, do not necessarily perform well on irregular waveforms such as sea ice [31]. Thus, the need arises to first identify the observed terrain based on the waveform shape and then applying the best performing retracker for this waveform class. The waveform classes used in this research are open ocean, leads and sea ice.

4-1-1 Classification Parameters

The three waveform classes, ocean, leads and sea ice, have distinct features as will be discussed in this section. These waveforms are classified based on the specular behavior of the maximum peak, the spread of the waveform and the number of peaks. In order to classify the waveforms, the pulse peakiness, the stack standard deviation, the stack kurtosis, the Gaussian fit on the maximum peak and the number of peaks in a waveform are used as parameters.

Before these parameters are discussed in more detail, it should be noted that all waveforms that have the maximum peak in the first 20 bins or the last 10 bins of the waveform are discarded. Early and late peaks indicate a noisy measurement and are therefore not further considered in the classification process.

Pulse Peakiness

The pulse peakiness, *PP*, is used to determine the peakiness of the maximum peak of the waveform. It is defined as the ratio of maximum power, P_{max}, and total power in the waveform, P_{wf} [29]. Eq. (4-1) shows that the more specular, thus narrow, the waveform is, the larger is the value of the pulse peakiness, *PP*, while never exceeding the value 1. The sum of the total power is taken from 1 to 128 in order to account for the number of Doppler beam samples per observation.

$$PP = max\left(P_{wf}\right)\sum_{i=1}^{128}\frac{1}{P_{wf}(i)} \tag{4-1}$$

Stack Standard Deviation

The stack standard deviation, *SSD*, is provided in the level 1b data acquired from European Space Agency (ESA). A given cell on the surface is observed by multiple beams that are used to form the waveform of that particular cell. The echos for the given cell that are used to determine the waveform are defined as stacks [6]. *SSD* expresses the standard deviation of the Gaussian distribution over the stack [32]. Eq. (4-2) shows the *SSD*, where $P(i)$ is the range integrated stack power for the number of beams, N [33].

$$SSD = \frac{1}{2}\frac{\sum_{i=1}^{N} P^2(i) \sum_{i=1}^{N} P^2(i)}{\sum_{i=1}^{N} P^4(i)} \tag{4-2}$$

Stack Kurtosis

Similarly to the *SSD*, the stack kurtosis is provided in the ESA's level 1b data set. The kurtosis expresses the peakiness with respect to a Gaussian distribution over the stack. A high kurtosis value indicates that the waveform has a high peakiness, which is to be expected for leads given its waveform shape. The stack kurtosis provided by ESA is computed for the individual echoes [32] and is computed by Eq. (4-3) with N being the number of beams and P being the stack power [33].

$$\gamma_2 = \frac{\frac{1}{N}\sum_{i=1}^{N}\left(P(i)-\mu\right)^4}{\left[\frac{1}{N-1}\sum_{i=1}^{N}\left(P(i)-\mu\right)^2\right]^2} - 3 \qquad \text{with} \qquad \mu = \frac{1}{N}\sum_{i=1}^{N} P(i) \tag{4-3}$$

Gaussian Fit

The final classification parameter is a Gaussian fit to the maximum peak. Here, a Gaussian distribution is fitted to the bin of maximum power and its two adjacent bins on each side. Only the maximum peak of the waveform is considered, as it covers its specular part, which is of relevance for the peak behavior of the waveform [34]. The Gaussian distribution, G, is expressed by Eq. (4-4) [35]. Here, A is the amplitude of the fit, $\bar{x}$ is the mean of the Gaussian fit and W is the width of the Gaussian fit which is determined by the standard deviation of the fit. The smaller the width of the Gaussian fit is, the more specular is the behavior of the waveform's peak. This improves in particular the determination of lead waveforms.

$$G = Ae^{-\frac{(\bar{x}-x)^2}{2W^2}} \tag{4-4}$$

Peak Number

The boundary values for the waveform classification were selected based on visual inspection of the waveform. As the shape of the open ocean waveform is well known, an iterative process led to the selected values. The ranges of the PP and the Gaussian fit width overlap with those defined for sea ice. One distinct characteristic of the open ocean waveform is the large width of the returned power which is reflected in a large standard deviation.

Due to the overlapping ranges in most of the classification parameters for ocean and sea ice waveforms, another criterion is introduced. By considering the number of peaks above a certain threshold, waveforms can be better distinguished and ambiguities can be further reduced. While for lead and ocean only one major peak is expected, sea ice waveforms consist of multiple peaks.

Table 4-1 shows the ranges for each previously mentioned parameters. The values of the parameters are determined by selecting multiple waveforms from each waveform class and assessing their statistical properties.

4-1-2 Validation

Besides the visual assessment of waveforms in different classes, a validation of the parameters is done using DTU Space data provided by [36]. Based on this data, a clear distinction can be made for leads, however, the ocean and sea ice class have overlapping regions of PP, stack kurtosis and the Gaussian

Table 4-1: The classification parameters of three waveform classes, lead, ocean and sea ice.

	Lead	**Ocean**	**Sea Ice**
Pulse Peakiness	>0.25	<0.05	<0.09
Stack Standard Deviation	<3	>40	4-35
Kurtosis	≥ 40	<0.9	<53
Gaussian Fit Width	0.5 - 0.9	<5.9	<6.4
Multiple Peaks		no peaks $\geq$ 0.4 P_{max} at min distance of 20 bins	multiple peaks $\geq$ 0.4 P_{max} at min distance of 20 bins

fit parameters. It becomes apparent that another constraint for these two classes is necessary. This has been implemented using the multiple peak characteristic. Moreover, the ranges of the classification by DTU Space are coherent with the parameters given in Table 4-1.

4-2 Open Ocean

The simplest case of a waveform is the one returned by open ocean. In the open ocean it is assumed that the presence of ice floes is below 5% [32]. Figure 4-3 shows the Arctic ocean on the left and a waveform classified as open ocean on the right. The statistical characteristics are in coherence with those given in Table 4-1.

The decisive classification parameter of open ocean is the number of peaks. If there are multiple peaks in the waveform at a distance of 20 bins or more that have a peak power of 40% of the maximum power, the waveform is not classified. The distance of 20 bins is selected in order to account for peaks in the trailing edge of the main peak.

4-3 Leads

Fractures in sea ice result in the presence of water in ridges as can be seen on the left in Figure 4-4. These ridges can have a diameter of hundreds of meters and run for kilometers [37]. The returned waveform of such a surface observation is a very narrow waveform called lead. A lead waveform and its characteristic values are shown in Figure 4-4. As the sea ice has a damping effect on the water, only minor waves caused by winds are present in the ridges. This results in predictable waveform behavior. During SAR observations of leads, the largest amount of power is received closest to the burst location. Consequently, leads that are observed ahead (behind) of nadir are reflected towards the front (back) [29]. These so-called off-nadir leads are not considered in this research.

[2] provides a reference value of *PP* to be larger than 0.18 and *SSD* to be smaller than 4. However, after inspecting lead waveforms, it was discovered that leads were wrongly classified to be leads using these criteria. In order to provide a clear distinction between sea ice and lead with respect to the stack standard deviation, the *SSD* value was set to be below 3. Concerning the pulse peakiness, the boundary value was increased as the maximum peak contains almost all power in the waveform and therefore, the specular return is ensured. This is also represented by the small width of the Gaussian fit of the subwaveform on the maximum peak.

4-4 Sea Ice

The presence of scattered ice floes in the Arctic ocean is classified as sea ice. Figure 4-5 shows an image of Arctic sea ice on the left and a returned waveform on the right. The distinct feature of multiple peaks in the waveform is clearly visible.

The values for the *PP* and *SSD* are based on reference values provided by [2]. The *SSD* has an upper boundary in order to limit the interference with the ocean classification, which is represented also in the wider spread of the ocean waveform compared to sea ice. As can be seen in Table 4-1, the constraint of multiple peaks is included to have a strong classification. For sea ice, there has to be

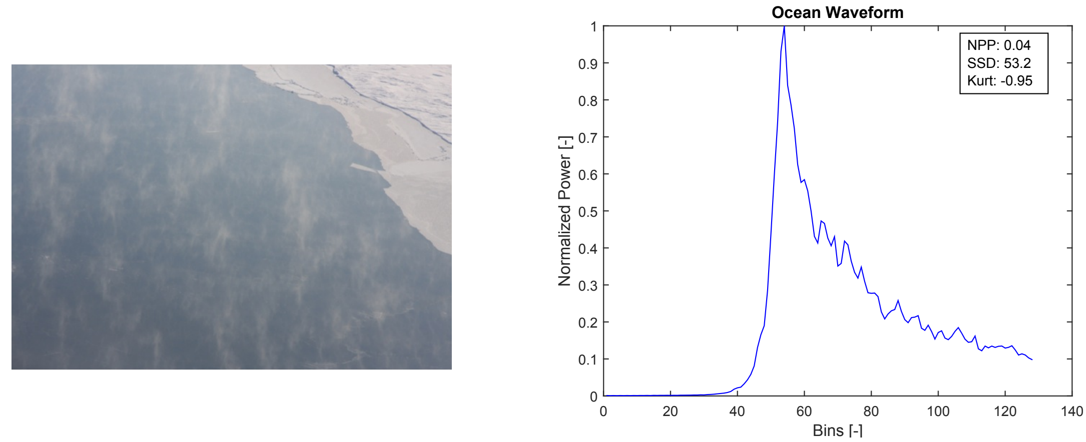

Figure 4-3: Ocean observation. *Left:* Arctic ocean next to an ice sheet [38]. *Right:* An open ocean waveform with its computed parameters.

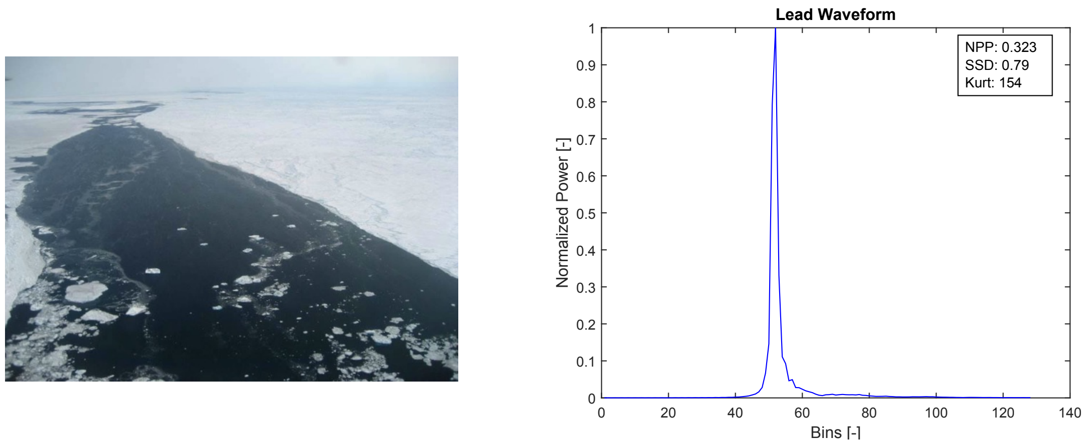

Figure 4-4: Lead observation. *Left:* Lead in the Arctic ocean [38]. *Right:* A lead waveform with its computed waveform parameters.

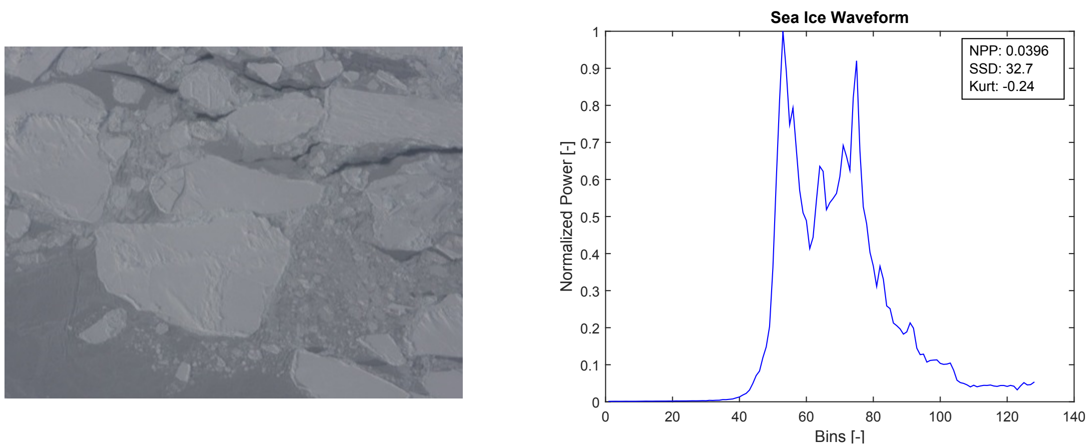

Figure 4-5: Sea ice observation. *Left:* Sea ice in the Arctic ocean [38]. *Right:* A sea ice waveform with its computed parameters.

another peak of at least 40% of the maximum waveform power at a minimum distance of 20 bins. This distance accounts for the trailing edge of the main peak and the leading edge of the secondary peak.

4-5 Seasonality

One characteristic of the Arctic region is its strong seasonality as shown in Figure 4-6. Here the ice concentration in the Kara Sea is shown per month in 2011. The data is provided by [39]. January is the month with the highest ice concentration, while the summer months August and September have the smallest ice concentration.

The effect of seasonality represented in Figure 4-6 can also be observed in the distribution of waveforms in a given class per month. Figure 4-7 shows the percentage of each waveform class for 2011. In all three waveform classes a clear seasonal tendency can be observed that is phase shifted.

Starting with the sea ice class, it can be observed that in the winter month January to April, the largest amount of sea ice waveforms are present, while in summer months (June to October) this percentage decreases significantly to below 10%. During spring (May to June), the sea ice melts and consequently fractures in the sea ice occur which results in an maximum number of leads. However, over the course of summer, the number of leads reduces as the melting continues leading to an increased number of ocean waveforms. During the winter months, which have a high concentration of ice, only few open ocean waveforms are available.

The significantly decreased number of leads in winter or ocean in summer, needs to be taken into consideration when computing the precision performance of the retrackers.

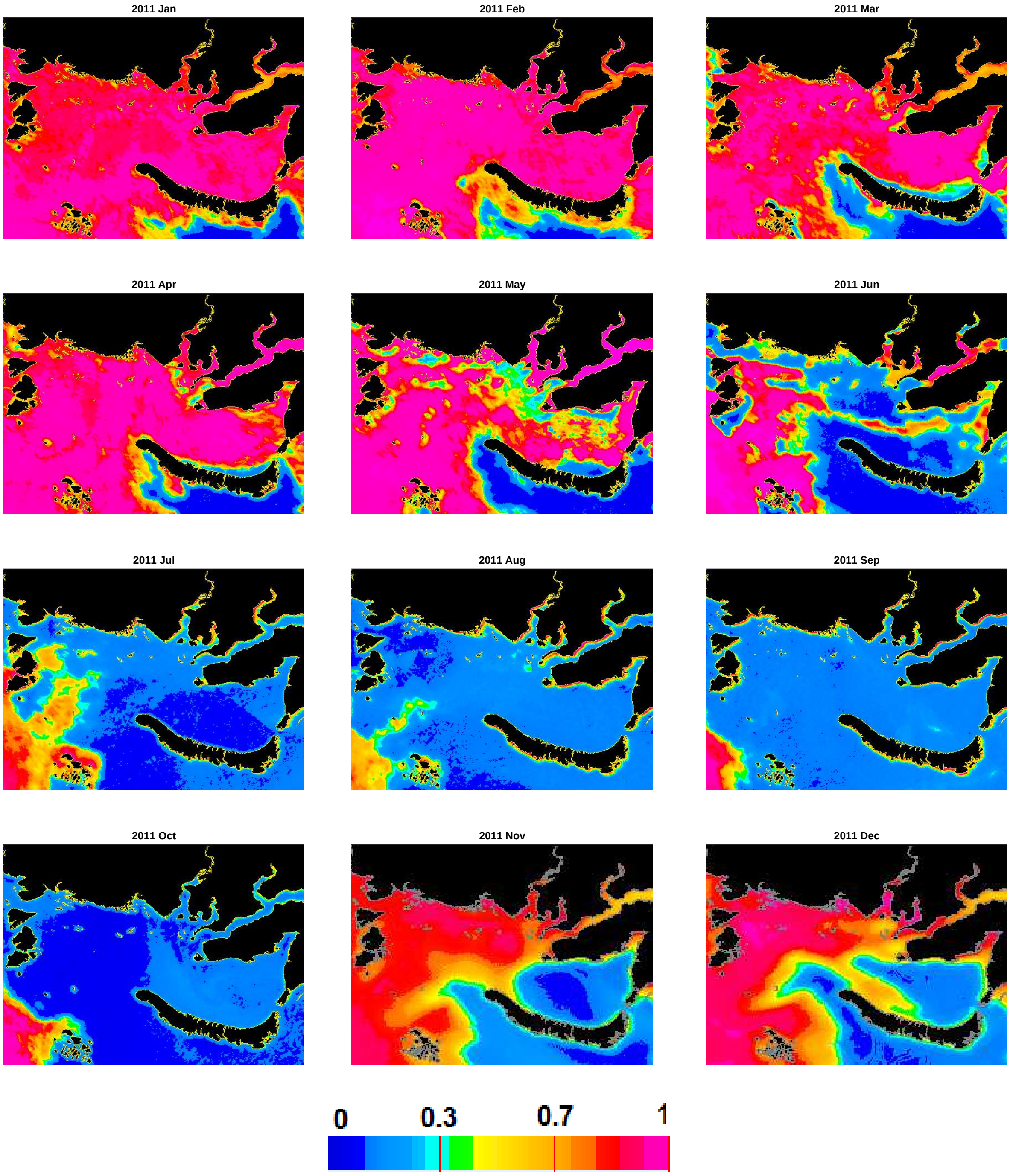

Figure 4-6: Sea ice concentration for the Kara Sea for 2011. Top row, left to right: January-March, second row: April-June, third row: July-September and bottom row: October-December. The data is taken from [39].

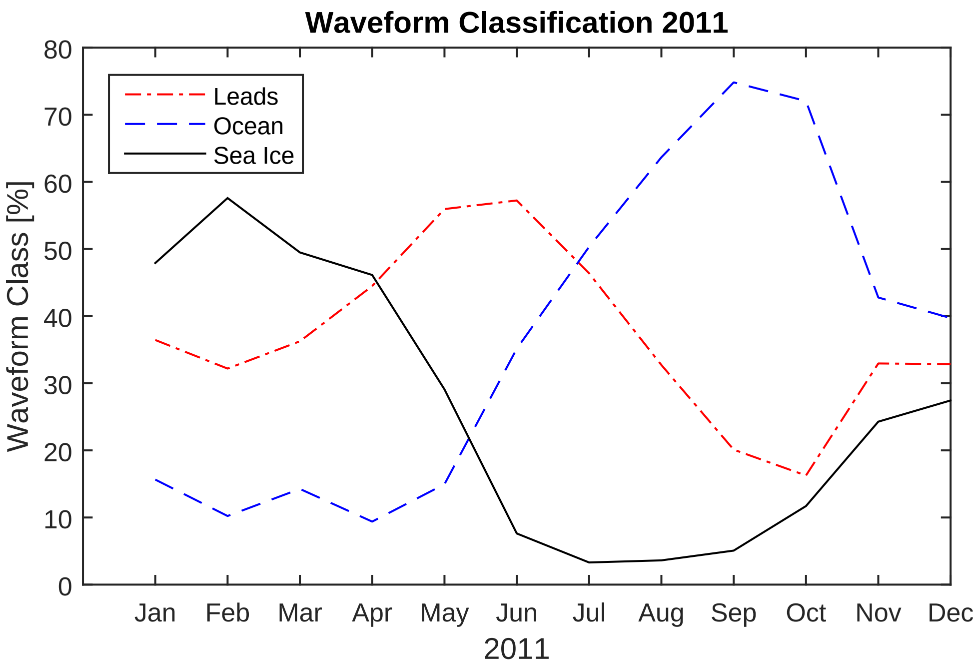

Figure 4-7: The percentage of waveforms per class on a monthly basis for 2011. This plot is based on Level 1b data using the classification parameters described in this section. Unclassified waveforms are not considered in this plot.

Chapter 5

Retrackers

The aim of retracking is to determine the point on the waveform that corresponds to the mean sea surface height. Generally, there are two main types of retrackers: empirical and physical ones. Physical retrackers are based on the scattering behavior in the microwave range [31], more specifically, the returned power includes the physical characteristics of the observed surface. Empirical retrackers on the other hand are either based on the statistical behavior of the waveform or fit an empirical function to the waveform. Therefore, empirical retrackers do not consider the surface conditions. Generally, physical retrackers are preferred over empirical retracker due to their ability to include surface characteristics.

In the following four retrackers and their working principle are introduced. First, the empirical primary peak Center of Gravity (PP COG) and threshold retracker are elaborated, followed by the physical SAMOSA retracker. Finally, the empirical CryoSat-2 retracker is discussed.

5-1 Primary Peak Retrackers

The primary peak retracker (PP) is an empirical retracker that only considers the waveform peak that contains the maximum power. It was developed by Maulik Jain at Denmarks Tekniske Universitet (DTU). Given the narrow SAR peak of the waveforms as has been shown in Section 4-1, the primary peak contains the main part of the reflected power. By considering only the primary peak and neglecting the remaining waveform, noise in the trailing edge caused by for example ice floes or coastal area are discarded [4].

In order to extract the primary peak of the waveform, the start and stop threshold of the subwaveform needs to be determined. To compute the start of the primary peak, a starting threshold is determined by comparing the power differences in alternating bins. The start threshold, TL_{start}, is determined using Eq. (5-1) with N being the total number of waveform bins, P_i is the power at a bin i and d_2^i is given by Eq. (5-2) [4]. If the start threshold is exceeded by a power difference for the first time in the waveform, the starting point is defined.

$$TL_{start} = \sqrt{\frac{(N-2)\sum_{i=1}^{N-2}\left(d_2^i\right)^2 - \left(\sum_{i=1}^{N-2} d_2^i\right)^2}{(N-2)(N-3)}} \tag{5-1}$$

$$d_2^i = P_{i+2} - P_i \tag{5-2}$$

Similarly, the stop threshold is computed by considering the power differences in consecutive bins as given by Eq. (5-3) and Eq. (5-4). The stop point is determined once the power difference is below the stop threshold. The issue that arises with this method is that the primary peak would be too small (1-3 bins). Therefore, additional two bins before the start and two bins after the stop point are also taken into computation of the primary peak. The number of extra bins has been determined based on experiments leading to the most optimal results [4].

As the start and stop threshold values are based on the standard deviation of the power difference in alternating and consecutive bins, respectively, this method is stable enough to identify the maximum peak in case it is not the primary one.

$$TL_{stop} = \sqrt{\frac{(N-1)\sum_{i=1}^{N-2}\left(d_1^i\right)^2 - \left(\sum_{i=1}^{N-2} d_1^i\right)^2}{(N-1)(N-2)}} \tag{5-3}$$

$$d_1^i = P_{i+1} - P_i \tag{5-4}$$

In order to reach an optimal performance of the retracker, the stop threshold value can be adjusted empirically. It was determined that a factor of 0.2 of the stop threshold provides the highest retracking performance of the primary peak retrackers [private communication Maulik Jain, 2015].

In the following the two versions of the primary peak are introduced. The PP Center of Gravity (COG) and the PP threshold retracker are a modification of the conventional Offset Centre of Gravity Retracker (OCOG) and the conventional threshod retracker, respectively.

5-1-1 Center of Gravity Retracker

The COG retracker fits a rectangle with the amplitude, A, and width, W, to the primary peak of the waveform. These parameters are computed using Eq. (5-5) and Eq. (5-6), where N is the total number of samples in the waveform, n_1 and n_2 are the start and end bins of the primary peak and P_i is the waveform power. Using the fitted rectangle as shown in Figure 5-2, the center of this rectangle, COG, can be computed which then results in the retracking point of the primary peak, C_{pp_cog} [4]. This is expressed using Eq. (5-7) and (5-8).

$$A = \sqrt{\frac{\sum_{i=n_1}^{N-n_2} P_i^4(t)}{\sum_{i=1+n_1}^{N-n_2} P_i^2(t)}} \tag{5-5}$$

$$W = \frac{\left(\sum_{i=n_1}^{N-n_2} P_i^2(t)\right)^2}{\sum_{i=1+n_1}^{N-n_2} P_i^4(t)} \tag{5-6}$$

$$COG = \frac{\sum_{i=1+n_1}^{N-n_2} iP_i^2(t)}{\sum_{i=1+n_1}^{N-n_2} P_i^2(t)} \tag{5-7}$$

$$C_{pp\_cog} = COG - \frac{W}{2} \tag{5-8}$$

5-1-2 Threshold Retracker

The primary peak threshold retracker is a modification of the conventional retracker used in pulse-limited altimetry. For more information on the conventional threshold retracker, the reader is referred to [40]. The primary peak threshold retracker determines the bin, i_{thres}, in which an a-priori power value, P_{thres}, has been exceeded. The optimal threshold value was shown to be 50% for 20 Hz CryoSat-2 data [4]. The threshold value is applied to the amplitude of the fitted rectangle to the primary peak, A, as has been computed by Eq. (5-5).

Based on the bin location and the respective power in that bin, the retracking point of the primary peak, C_{pp_thres} can be computed by Eq. (5-9) using a linear interpolation between the two bins where the threshold value has been reached, P_{ithres} [4]. Eq. (5-9) is derived by computing the slope between the two outer points, thus $ithres - 1$ and $ithres$, and setting it equal to the slope between $ithres - 1$ and C_{pp_thres}. Figure 5-1 shows the geometry of this linear interpolation.

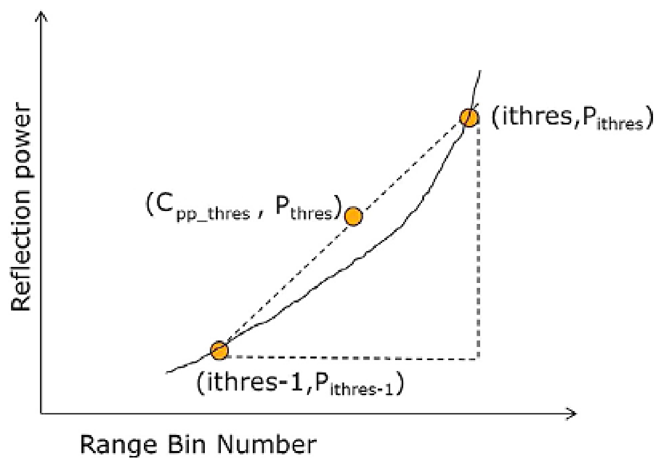

Figure 5-1: Linear interpolation scheme to determine the retracker point for the primary peak threshold method [4]. Eq. (5-9) is based on the geometry shown here.

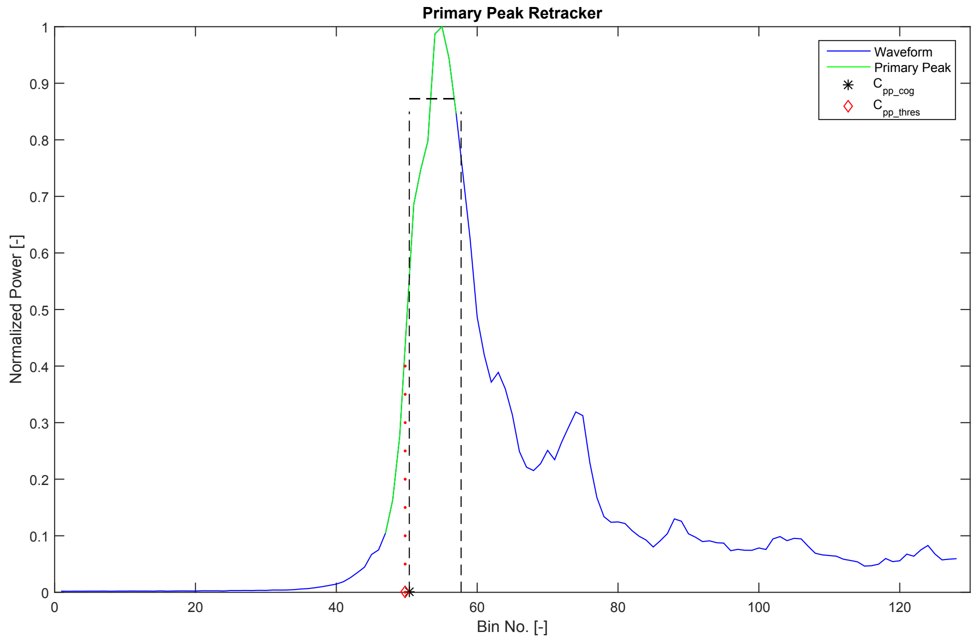

Figure 5-2: Geometry of Primary Peak Retrackers. The blue line shows the waveform, the green line indicates the extracted primary peak. The black dotted line shows the rectangle that is fitted to the primary peak. The black asterisk and red diamond show the retracking point of the COG and threshold retracker, respectively.

$$C_{pp\_thres} = i_{thres} - 1 + \frac{P_{thres} - P_{thres-1}}{P_{thres} - P_{thres-1}} \tag{5-9}$$

Figure 5-2 shows the geometry of the primary peak retrackers. The blue line indicates the waveform of the reflected power, while the primary peak is given in green. The primary peak is calculated based on the previously presented equations. Furthermore, the retracking point for both the PP threshold retracker (red) and the PP COG (black). Both primary peak retrackers are robust, empirical retrackers which are able to deal in particular with irregular waveforms.

5-2 SAMOSA Retracker

The SARL Altimetry MOde Studies and Applications (SAMOSA) retracker has been developed by Starlab and National Oceanography Centre (NOC) in the scope of the SAMOSA project [41]. It is a physical, full waveform retracker that provides a closed-analytical expression of the waveform and exists in different versions as will be explained later on.

In order to retrack a waveform in the open ocean, the Brown waveform model can be adjusted to represent SAR altimetry. Taking into account the dependency on Doppler bins, the power waveform, P can be computed by Eq. (5-10) [42],

$$P(x_i, t) = p_{FS0}(x_i, t) * \mathrm{RIR} * q(t) \tag{5-10}$$

where p_{FS0} is the ideal flat surface response given in Eq. (5-11), *RIR* is the range impulse response, which is a sinc^2 function and $q(t)$ represents the surface height probability density function determined by Eq. (5-12). A Gaussian distribution is assumed in the determination of the surface height probability density function, leading to an exponential equation.

$$p_{FS0}(x_i,t) = \int_{x_i-\frac{\delta x_{bin}}{2}}^{x_i+\frac{\delta x_{bin}}{2}} \int_{t-\frac{\delta t}{2}}^{t+\frac{\delta t}{2}} G_{Ant}^2(x,t)\sigma_0(x,t)dxdt \tag{5-11}$$

$$q(t) = \frac{2c}{\sqrt{2\pi}\mathrm{SWH}} \exp\left(\frac{-t^2}{2(\mathrm{SWH}/(2c))^2}\right) \tag{5-12}$$

In the above equations G_{Ant} represents the antenna gain, σ_0 is the backscatter coefficient, t is the sampling time interval, c indicates the speed of light and *SWH* is the significant wave height.

These equations serve as a basis for the SAMOSA physical retracker, meaning that the waveform characteristics are related to the geophysical parameters [43]. SAMOSA is a fully analytic model with two independent variables: Doppler frequency and the time delay [44] that retracks the full waveform.

The SAMOSA retracker implements surface and instrument parameters in its retracking algorithm: the skewness in the sea surface height, *SSH*, elliptical antenna gains, roll and pitch biases, vertical speed, sea surface slope and the squared point target response in this retracking algorithm [44].

In order to derive a closed-form expression that models the full waveform based on the equations above, further simplifications are done. By assuming a negligible skewness, a 1% error in the determination of the power is introduced leading to the total backscattered power at a certain cell (k, l) by Eq. (5-13) [43].

$$P_{k,l} = KB_{k,l}\sqrt{g_l}\left[f_0\left(g_l\kappa\right) + T_{k,l}g_l\sigma_s^2 f_1\left(g_l\kappa\right)\right] \tag{5-13}$$

with

$$K = \frac{\lambda_0^2 N_b^2 L_x L_y}{4\pi h^4}\sqrt{2\pi}A_g^2\sigma_g^2 \tag{5-14}$$

$$g_l = \left[\sigma_g^2 + \left(2\sigma_g l L_x^2/L_y^2\right)^2 + \sigma_s^2\right]^{-1/2} \tag{5-15}$$

B and T are functions that are used for a linear approximation of the antenna gain and radar cross section product, κ is an approximation introduced in the range cell mitigation correction. Furthermore, N_b is the number of pulses per burst, L_x is a function of the Pulse Repetition Frequency (PRF) and the center frequency, while L_y is a function of the usable pulse length and the altitude, h. A_g and σ_g are parameters defined by the Gaussian approximation during the along-track Fast Fourier Transform (FFT), σ_s indicates the standard deviation of the sea height mean and λ_0 is the wavelength. For more information on the variables as well as the derivation of $P_{k,l}$, the reader is referred to [43].

The term f_0 and f_1 can be generally expressed by Eq. (5-16) with η, ξ and v being the Bessel function parameters [43]. Looking back at Eq. (5-13), it can be seen that a series in terms of the parameter f is present. By including both zero and first order terms, the SAMOSA2 retracker model is build. When the first and higher order terms are discarded, a simplified version of the SAMOSA2 retracker is created which is called SAMOSA3 [44]. The assumption of discarding f_1, will result in the introduction of an error, however, the f_1 term is only of importance if the *SWH* is larger than two meters [43].

$$f_n(\eta) = \int_0^{\infty} \left(v^2 - \xi\right)^n e^{-\left(v^2-\xi\right)^2/2} \tag{5-16}$$

Furthermore, it should be noted that the sinc^2 of the *RIR* as shown in Eq. (5-10) is approximated by an exponential function in the analytic SAMOSA model. This will lead to the result of the single-look waveform. In order to achieve a multi-look function, a stack of single-look waveforms is averaged [45].

Looking at SAMOSA3, the retracker is operated in two different modes: lead and ocean. In the lead mode the retracking position and surface roughness are fitted, while the significant wave height is assumed to be zero. This is a valid assumption since the ice sheets damp waves significantly and only minor wind generated waves are present. The ocean modes fits the *SWH* and retracking position [45]. In both cases a damped least squares method is applied [37].

The pearson correlation coefficient determines the mode of the waveform. Eq. (5-17) shows the definition of the pearson correlation coefficient. Here, E[ab] represents the cross-correlation between two random variables a and b, σ_a and σ_b is the standard deviation of a and b, respectively [46]. It should be noted that the squared pearson correlation coefficient is used to determine the linear correlation between two random variables with its value being between 0 and 1. The higher the squared pearson correlation coefficient is, the more linearly correlated are the two variables [46].

$$\rho(a,b) = \frac{E[ab]}{\sigma_a \sigma_b} \tag{5-17}$$

The pearson correlation coefficient is in particular useful to analyze the waveform as it can be expressed in different domains such as the time and frequency domain [46].

In the ocean mode of SAMOSA the pearson correlation coefficient between the real and modeled waveform has to be above 0.9 in order for the waveform to be considered ocean. In the lead mode, the pearson correlation coefficient needs to be above 0.95 to be classified as a lead [45]. The data provided by SARvatore Grid Processing On Demand (GPOD) that is used in this research is fitted to all waveform classes without previous filtering or waveform classification [18].

5-3 CryoSat-2 Retracker

The CryoSat level 2 product includes the retracked waveform using the CryoSat/ESA retracker. Level 2 data is produced by correcting level 1b data for geophysical corrections and by applying the retracker for every mode separately. The empirical ESA retracker is based on a full waveform fitting. However, while [13] provides the mathematical final descriptions of the retracker, there is no derivation available of those equations.

The retracker is based on fitting a function to the multi-look echo using a least squares approach. The used function, f_Ψ, is given by Eq. (5-18). The argument parameters of f_Ψ will be fitted in order to determine the SAR waveform [13] with t_p representing the compressed pulse duration.

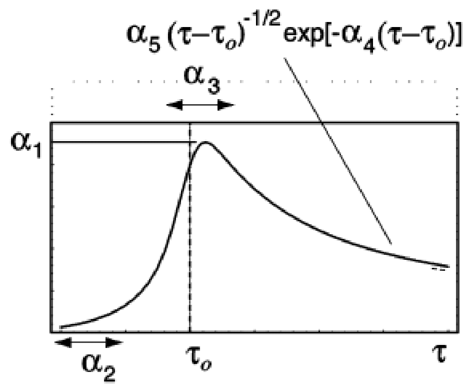

Figure 5-3: The physical meaning of the fitted CryoSat-2 parameters on the waveform as a function of time τ [13].

$$f_\Psi(t;a,\sigma,t_0,c,\alpha,n) = a\exp\left(-h^2\left(t/t_p\right)\right) \tag{5-18}$$

In Eq. (5-19), s, a_2 and b are parameters that are eliminated as h and the first derivative of h is continuous [13]. The fitting parameters of the waveform are shown in Figure 5-3, where

- α_1 is the maximum power
- α_2 is the leading edge duration
- α_3 is the peak duration
- α_4 is the contribution of antenna pattern to trailing edge
- α_5 is the amplitude of the trailing edge

$$h(s) = \begin{cases} \frac{1}{10}(s-s_0) - 2.5 + \frac{n\sigma}{10} & s < s_0 - n\sigma \\ b_0 + b_1\left(s - s_0 - \frac{\sigma}{2}\right) + b_2\left(s - s_0 - \frac{\sigma}{2}\right)^2 + b_3\left(s - s_0 - \frac{\sigma}{2}\right)^3 & s_0 - n\sigma < s < s_0 - \frac{\sigma}{10} \\ \frac{1}{\sigma}\left(s - s_0 - \frac{\sigma}{2}\right) & s_0 - \frac{\sigma}{10} < s < s_0 + \frac{\sigma}{2} \\ \frac{1}{\sigma}\left(s - s_0 - \frac{\sigma}{2}\right) + a_2\left(s - s_0 - \frac{\sigma}{2}\right)^2 + a_2\left(s - s_0 - \frac{\sigma}{2}\right)^3 & s_0 + \frac{\sigma}{2} < s < s_0 + 2\sigma \\ -\log^{1/2}\left[\frac{c\exp(-\alpha(s-s_0))}{a(s-s_0)^{1/2}}\right] & s > s_0 + 2\sigma \end{cases} \tag{5-19}$$

Chapter 6

Retracker Performance

The performance of a retracker is defined by its accuracy and precision. Figure 6-1 shows how these characteristics are specified. While accuracy determines the discrepancy between the mean of the conducted measurements and its reference value (e.g. from tide gauge data), precision is defined by the width of the distribution of the measurements and is therefore also called reproducibility [47]. Consequently, the accuracy is the difference in mean from observations and reference data, while precision is based on the standard deviation of the measurements. It becomes apparent that computing the accuracy of retrackers is more challenging due to the limited continuous in-situ data in the Arctic region. Tide gauges are predominantly present in the coastal area and only few gauges can be observed away from the coast.

Both the precision and the accuracy will be assessed based on the behavior of the sea level anomaly (SLA). The sea level anomaly is used for performance analysis as the sea surface height and signal corrections have been subtracted from the returned signal. Thus, the dominating bias that is left when comparing two sea level anomaly values is the retracker bias. Eq. (6-1) shows the computation of the sea level anomaly. Here, H is altitude of the spacecraft with respect to the reference ellipsoid, R_{cor} describes the range corrected for geophysical and range discrepancies. MSS represents the mean sea surface.

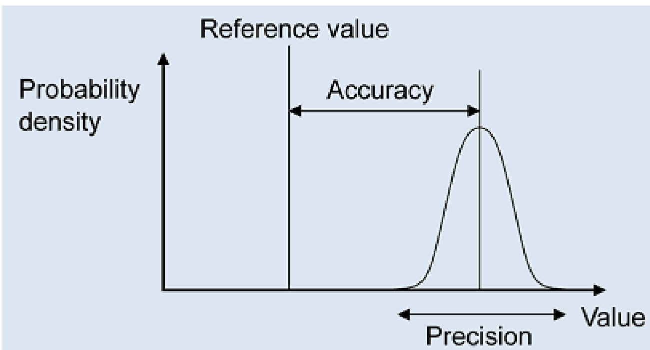

Figure 6-1: The definition of accuracy and precision that will be used to analyse and evaluate the retracker performance [48].

$$SLA = H - R_{cor} - \text{MSS} \tag{6-1}$$

Within this chapter, the precision and accuracy of the retrackers described in Chapter 5 is discussed. First the precision performance is discussed in Section 6-1 followed by an accuracy analysis with respect to tide gauge and Envisat data. Finally, the optimal retracker is presented based on the precision and accuracy performance.

6-1 Precision

The precision performance is determined based on the mean standard deviation per month. For this purpose, the 1 Hz sea level anomaly is computed by selecting the level 1b 20 Hz data over a one second interval. The variations in the selected 20 Hz data points over a one second interval represents the standard deviation, σ_{SLA}. By computing the mean of the standard deviation over the test region and the desired time period, the mean standard deviation is determined. Figure 6-2 shows the mean standard deviation for the months of 2011 for the individual waveform classes ocean, leads, sea ice and unclassified.

Considering the ocean waveforms, a higher precision, thus lower standard deviation, is observed for all retrackers in summer (June to September), compared to winter (November to April). The behavior of all retrackers show a direct relation with the percentage of ocean waveforms as shown in Figure 4-7. Thus, the precision is higher in the summer months, where the number of ocean waveforms is significantly higher than for the remaining months. The physical retracker SAMOSA has the highest precision performance for ocean waveforms for all month except April. In April the Primary Peak Center of Gravity (COG) retracker outperforms SAMOSA. When comparing the two primary peak retrackers, it can be observed that the COG outperforms the threshold retracker in all month for ocean. However, it should be noted that for all waveform classes, the two retrackers behave very similar with only small deviations. The least precise retracker for ocean waveform is the ESA retracker that follows the shape of the other retrackers, however, at an offset.

For the irregular waveforms of sea ice and leads, the empirical primary peak retrackers have the most precise performance. SAMOSA performs the worst for leads, however, it should be noted that the standard deviation values are significantly lower (2 - 4.3 cm) compared to the ocean waveforms (4 - 16 cm). Furthermore, the shapes of the lead waveforms are similar for all retrackers, though given at an offset.

The precision performance of sea ice indicates that in summer months, SAMOSA is the best retracker and that additionally, the ESA retracker also performs significantly better in that time frame. However, this result is strongly dependent on the number of observations in these months. Due to the high seasonality, very few ice observations are present in the test region from June to October. Therefore, fewer observations are used to compute the variation in the 1 Hz data, resulting in less volatility in the data. August represents the data misalignment for the entire summer months, as there are 62 SAMOSA, 8 ESA, 163 and 196 COG and threshold, respectively 1 Hz standard deviation data points.

Consulting Figure 4-7, January to May have a high sea ice content. Cross referencing this with the precision of the retrackers, the primary peak retrackers significantly outperform SAMOSA and ESA retracker, showing their ability to cope with irregular waveforms. It should be noted that the mean

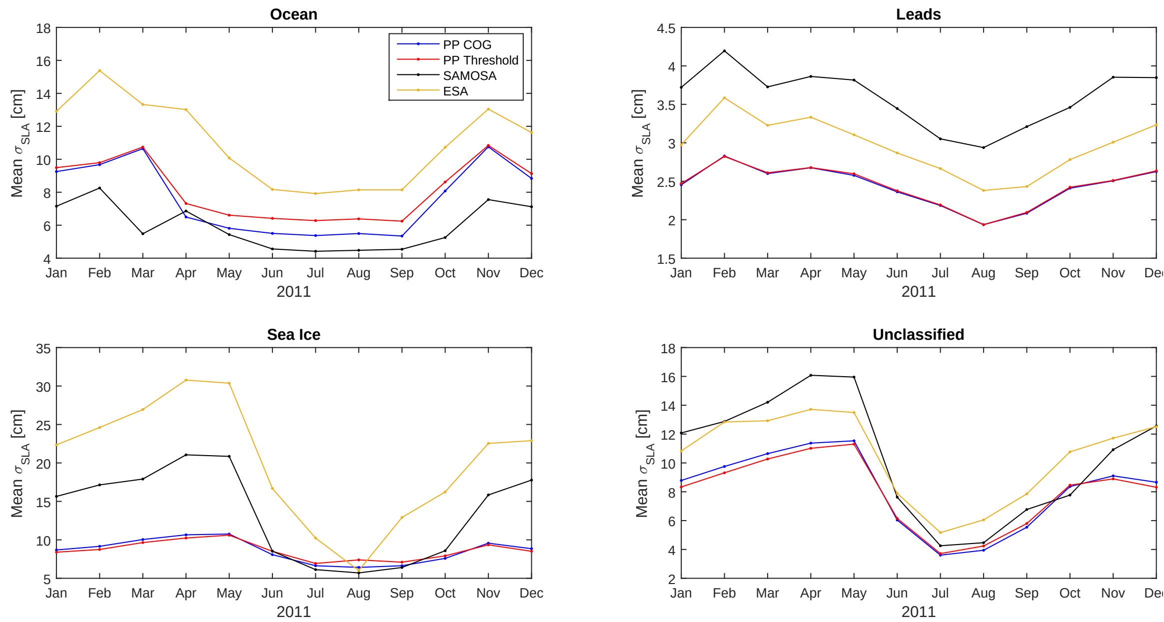

Figure 6-2: Precision performance of the primary peak center of gravity and threshold retracker, SAMOSA and ESA retracker for four different waveform classes: ocean, leads, seaice and unclassified. The precision is determined on a monthly basis for 2011 based on its standard deviation. Note the different scales of the vertical axis.

standard deviation range, is the highest compared to all other waveform classes. This is due to the complex waveform shape of sea ice which cannot be represented by the algorithms of the retrackers.

Finally, the unclassified waveforms show a similar behavior of all retrackers with a comparable value range to the ocean waveforms. It is difficult to draw any conclusions from this plot, as the data shown could be close to lead, ocean or sea ice, meaning that the precision is significantly varying. However, a seasonal trend can be observed that is related to the percentage of sea ice observations, thus high standard deviation in winter months and low standard deviation in summer months. A reason for this could be that waveforms were not classified as sea ice as they violated at least one constraint, however, have very close behavior to classified sea ice. Furthermore, the sea ice observations has the highest standard deviation and consequently the highest impact on the overall precision performance. Generally, it can be concluded that the primary peak retrackers are able to cope best with unclassified, irregular waveforms in terms of precision, while the physical SAMOSA retracker and the empirical ESA retracker perform worse.

Figure 6-3 shows the precision for the months of 2011 for the waveform classes ocean, leads and sea ice combined. Unclassified waveforms are not considered as their performance is unpredictable for the given research.

For all four retrackers, a clear seasonal tendency can be observed with a lower precision in the winter months (January to May) and a higher precision in the summer months. The reason for this is the composition of waveform classes. In summer ocean waveforms are predominant, which are predictable and well retrackable waveforms, while in winter mainly sea ice observations are present, resulting in irregular waveform shapes. As has been shown before, SAMOSA is not able to precisely retrack sea ice data, which is presented by a worse performance in the winter months. From August to October

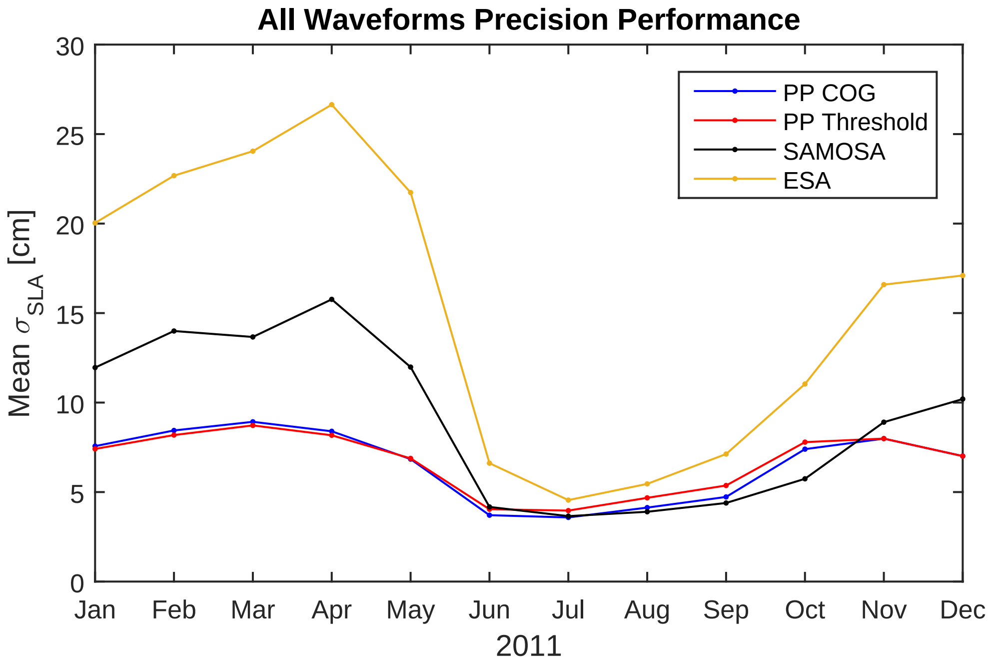

Figure 6-3: Precision performance of the primary peak center of gravity and threshold retracker, SAMOSA and ESA retracker. The precision is determined on a monthly basis for 2011 based on its standard deviation.

SAMOSA is overall the best retracker in terms of precision which agrees with its good performance for ocean waveforms.

The primary peak retrackers outperform the other two retrackers for most parts of the year. While in the winter month the threshold retracker performs better, which is representative for its good sea ice precision as shown in Figure 6-2, COG has a higher precision in the summer month as a consequence of its good open ocean retracking.

In general, the precision performance plot underlines the expected behavior. The primary peak retracker are able to cope best with irregular data, as its empirical approach only focuses on a sub-waveform on the primary peak (see Figure 5-2) and therefore does not take noise outside of the primary peak into consideration. In particular irregular waveforms have a significant amount of noise in the waveform due to smaller peaks form off nadir ice observations.

The ESA retracker provides a poor precision performance over the entire year, in particularly in winter. While the ESA retracker is also an empirical retracker, it was found that it performs significantly worse than the other retrackers. The reason for this lies in the design of the retracker, as it fits an exponential function to the entire waveform (see Section 5-3). While the trailing edge is also described by an additional exponential function, the ability of this retracker to cope with multiple peaks or noise in one waveform as is the case for sea ice observations is limited.

SAMOSA is the only physical retracker analyzed in this research. Similarly to the ESA retracker, SAMOSA also retracks the full waveform, however, it includes geophysical parameters in the computation of the retracking point (see Section 5-2). By taking into consideration the surface properties of the retracked surface. While this approach is in particular over open ocean effective, it is not able to deal with irregular waveforms that are affected by noise.

6-2 Accuracy

In order to assess the accuracy performance, benchmark data needs to be available. However, due to the high latitudes of the test region only little reference data from in-situ observations or other altimeters is accessible. In this section, in-situ data provided by tide gauges will be analyzed and their limitations in this research is assessed. Further, altimetry data provided by ESA's Envisat satellite is used to compute crossovers with CryoSat-2.

6-2-1 Tide Gauge Data

Tide gauges are used to provide a long term sea level measurement at a given location. As tide gauges are located in coastal areas, the sea level is measured with respect to the local land as a reference [49]. However, the tide gauge measurements need to be placed in an absolute reference to compensate for sea and land motion as will be explained in this section.

For the given test region, three tide gauges are available that contain measurements for 2011. All of the tide gauges are located in the Russian Federation: Vise, Izvestia Tsik and Stelegova. Figure 6-4 shows the location of the tide gauges with respect to the test region that is used in this research.

The tide gauge data is provided by Permanent Service for Mean Sea Level (PSMSL) and is given in a revised local reference frame (RLR) that varies for each tide gauge location. Here, the mean of the first year sea level observations is set as a reference above an arbitrary benchmark of about 7 m [50]. For Vise that is the mean sea level in 1954, for Izvestia Tsik (ITO) and Sterlegova the mean sea level in 1953 and 1950, respectively, are used. Consequently, the measurements obtained at a given tide gauge is a relative measurement with respect to this benchmark. The offset of the zero mean sea level in the first year and the benchmark varies from tide gauge to tide gauge, but is always around 7 m [50].

The tide gauge data retrieved from PSMSL provides the monthly mean sea level, which is based on daily observations in a four hour interval [50].

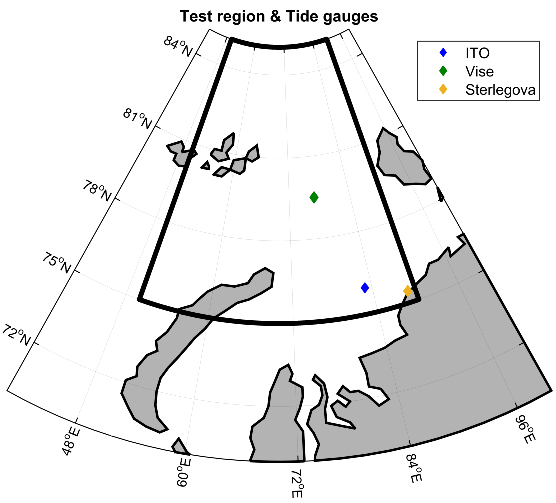

Figure 6-4: The test region and the tide gauge locations.

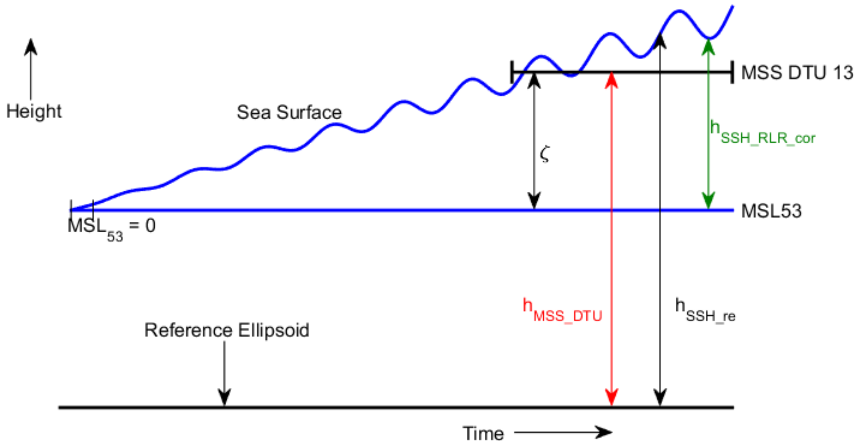

Figure 6-5: The tide gauge system geometry over time. MSL_{53} shows the local reference to which the tide gauge observations are measured. It is based on the Mean Sea Level of 1953 in this case. The tide gauge returns the height of the sea surface with respect to the RLR, $h_{SSH\_RLR\_cor}$. The mean sea surface with respect to the TOPEX/Poseidon reference ellipsoid is represented by h_{MSS_DTU}. Finally, ζ is the height between mean sea surface DTU13 and the RLR, MSL_{53}, used to compute the sea surface height in a global reference frame, h_{SSH_re}.

In order to compare the local tide gauge measurements with altimetry data, the tide gauge observations need to be adjusted to the land motion and sea level rise since the year of its first observation. This adjusted sea level is then related to the reference ellipsoid of the satellite. Figure 6-5 shows the geometry of the adjustments used to obtain tide gauge data with respect to the same absolute reference as CryoSat-2.

The sea surface height at a tide gauge location given with respect to the reference ellipsoid of TOPEX/-Poseidon, h_{SSH_re}, can be expressed as a function of the local tide gauge measurements. Eq. (6-2) shows this relation, where h_{MSS_DTU} is the mean sea surface (MSS) DTU13 with respect to the TOPEX/Poseidon reference ellipsoid and $h_{SSH\_RLR\_cor}(t)$ is the local sea level measurement of the tide gauge over time corrected for Glacial Isostatic Adjustment (GIA) as well as the inverse barometric effect. Finally, ξ is the difference between the sea level mean of the tide gauge measurements during the years taken into account in the DTU13 MSS model with respect to RLR.

$$h_{SSH\_re} = h_{SSH\_RLR\_cor}(t) + h_{MSS\_DTU} - \xi \tag{6-2}$$

Glacial Isostatic Adjustment is an effect caused by the reaction of the solid Earth to the redistribution of ice and water, affecting the sea level as well as the gravity field [51]. This results in a vertical land movement, influencing the sea level determination.

The correction for GIA and the inverse barometric effect since the reference year of a tide gauge has been computed for different locations in [52]. Table 6-1 shows the corrections for the three tide gauges that account for the time since the reference year.

DTU13 is a high resolution mean sea surface model that contains 20 years of altimetry data for a period from 1993 - 2012 [53]. Therefore, the measurements at each tide gauge from 1993 - 2012 are used to determine the mean over that period for a given location, ξ.

Based on the sea surface height with respect to the TOPEX/Poseidon reference ellipsoid, the *SLA* can be computed as shown in Eq. (6-3). As can be seen, the mean sea surface component is discarded

Table 6-1: The GIA and inverse barometric correction for the three tide gauges used in this research [52].

	Izvestia Tsik	Vise	Sterlegova
GIA [mm/year]	0.58	2.66	0.51
Inverse Barometric [mm/year]	0.30	0.29	0.55

when computing the *SLA* by combining Eq. (6-2) and Eq. (6-3). The difference in reference ellipsoid between the CryoSat-2 data and the tide gauge data is also eliminated in Eq. (6-3), because DTU13 is applied and therefore, the sea level anomaly is computed as the deviation to the mean sea surface.

$$SLA = h_{SSH\_re} - h_{MSS\_DTU} \tag{6-3}$$

The accuracy performance of the four retrackers with respect to the tide gauge data during 2011 is shown in Section 6-2-3.

A final remark concerns the location of the tide gauge data. The selected tide gauges are located in coastal areas of islands, however, coastal regions are observed by CryoSat-2 in SARIn mode as described in Section 2-2. Therefore, the location of the in-situ data is actually not included in the data set as it is not observed in SAR mode. This limits the extend to which the accuracy is represented by tide gauge observations.

6-2-2 Envisat Data

Another method to determine the accuracy of retrackers is by analyzing crossovers with other altimeter missions. Within this research, ESA's Envisat is used as a reference satellite. Given its polar orbit with an inclination of 95.55°, it reaches latitudes up to 84.45° and therefore provides sufficient crossover opportunities with CryoSat-2. Envisat's mission ended in April 2012 when contact was lost with the satellite [54]. For the time period that is analyzed in this research, the year 2011, sufficient crossover points are available to evaluate CryoSat's accuracy.

In order to minimize the variation in *SLA*, the Envisat reference tracks are constrained to 15 days before and after the CryoSat track occurs. The Envisat data is retrieved from Radar Altimeter Database System (RADS) [55]. Since the crossover data by Envisat does not necessarily coincide with a measurement of CryoSat, the Envisat data is interpolated to provide data at a given location.

RADS provides the data with respect to the TOPEX/Poseidon reference ellipsoid, while CryoSat-2 uses WGS84 (World Geodetic System) as a reference ellipsoid [6]. The difference in reference ellipsoid is caused by different radii and flattening coefficients used. The reference ellipsoid offset is latitude dependent and is about 70 cm [7]. Therefore, the Envisat data is corrected for this offset. For more information on how the correction is applied, the reader is directed to Appendix A.

Another aspect that is considered in the crossover analysis is the resolution. The Envisat data is based on a 1 Hz resolution, while the CryoSat-2 data used in this research has 20 Hz resolution. In order to create 1 Hz CryoSat-2 observations, the *SLA* is averaged over a 1 second interval. It does not necessarily mean that 20 observations are used to compute the 1 Hz value, as the number of observations in one second can differ depending on previous filtering. By comparing 1 Hz data,

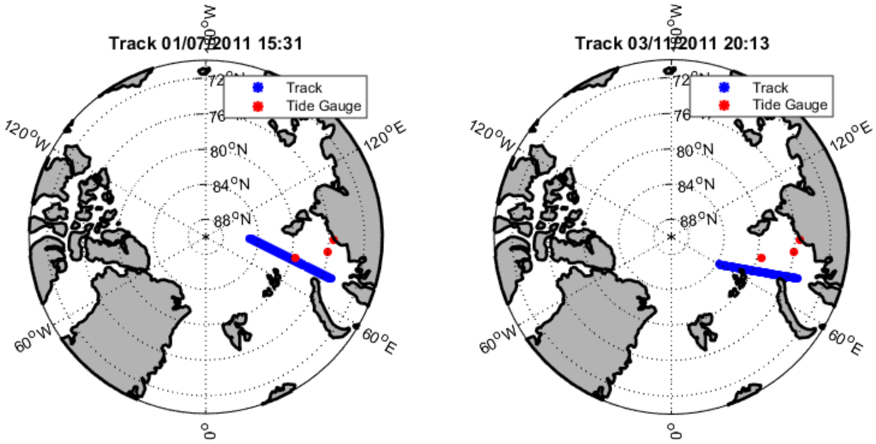

Figure 6-6: Footprint of the two tracks (blue) and the tide gauge locations (red). *Left:* Track on July 1, 2011. *Right:* Track on November 3, 2011.

similar resolutions are achieved as both satellites orbit at similar altitudes (CryoSat-2: 717 km [6], Envisat: 782 km [56]).

The accuracy is assessed based on two tracks to account for the different seasonal conditions: one in July and one in November. The footprint of the tracks is indicated in Figure 6-6.

The sea level anomaly of four retrackers using CryoSat-2 data and the Envisat crossover data is shown in Figure 6-7. For the sake of completeness the monthly average of tide gauge data of Sterlegova (latitude: 75.42°N), Izvestia Tsik (latitude: 75.95°N) and Vise (latitude: 79.5°N) is indicated. The observed data points belong to the ocean waveform class. The *SLA* of the primary peak retrackers as well as some SAMOSA observations are very close together, while the ESA retracker is at an offset. Based on the Envisat data, the ESA retracker performs best, though still with an offset of about 40 cm.

The right plot of Figure 6-7 shows the difference in time between the CryoSat-2 and Envisat observation. With a difference of up to 14 days, a significant deviation in *SLA* might be the consequence. However, it seems that the Envisat *SLA* is set around 80 cm independent of It is difficult to draw a conclusion on the accuracy behavior of the different retrackers based on Envisat data for this track.

Additionally, no clear accuracy determination can be concluded from the tide gauge data, as they are located in between the primary peak retrackers and SAMOSA. Furthermore, the tide gauge data plotted in the figure is the monthly mean for July, thus, it does not necessarily correspond to one temporal observation of an altimeter.

The second crossover analysis is shown Figure 6-8 and leads to similar results as the July track. Envisat's *SLA* values are at an offset with respect to the retrackers used for the CryoSat-2 data. However, the general behavior of the data over time is the same for both CryoSat-2 and Envisat data. It should be noted though that the difference in crossover time is larger compared to the previous track, while the difference in *SLA* remains similar.

All three tide gauge data behave similarly to the July track and their behavior will be discussed in more detail in Section 6-2-3.

The two crossovers tracks with Envisat show that it is difficult to assess the accuracy of the four retrackers. In particularly, the time difference between the CryoSat-2 track and the crossover points of

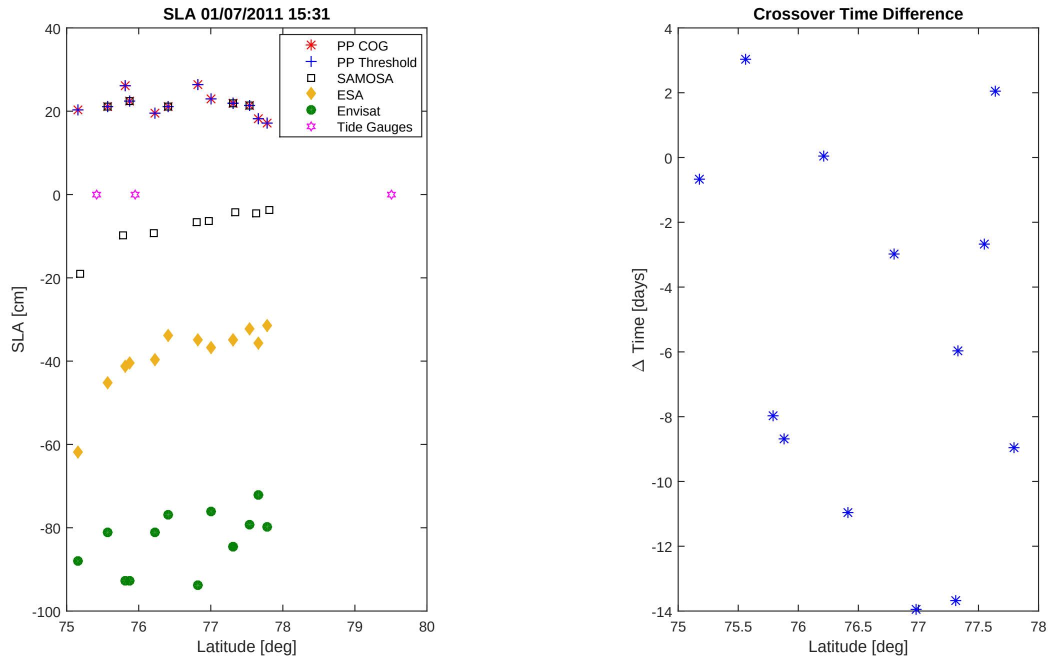

Figure 6-7: Track analysis 01/07/2011. *Left:* The sea level anomaly as a function of latitude of four retrackers using CryoSat-2 data (PP COG, PP Threshold, SAMOSA and ESA retrackers) and Envisat data. *Right:* Time difference between CryoSat-2 measurements and Envisat crossover data points.

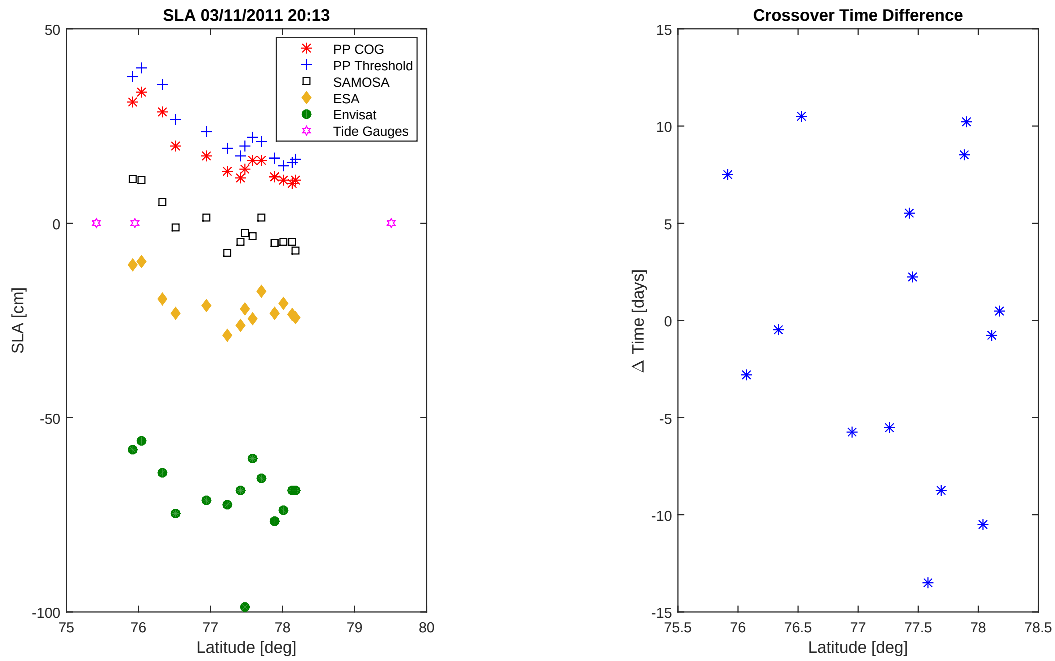

Figure 6-8: Track analysis 03/11/2011. *Left:* The sea level anomaly as a function of latitude of four retrackers using CryoSat-2 data (PP COG, PP Threshold, SAMOSA and ESA retrackers) and Envisat data. *Right:* Time difference between CryoSat-2 measurements and Envisat crossover data points.

Envisat of up to 15 days, has an influence on the representative means of this accuracy determination. Besides the time constraint of the data also other aspects play a role in the evaluation of Envisat data for accuracy determination as will be discussed in the following.

Eq. (3-2) showed which corrections are applied to the observed range in order to obtain the corrected range. It becomes apparent that the correction models and reference ellipsoid applied are the same for the two missions. Therefore, the origin of a potential bias in the crossover analysis is elsewhere. One uncertainty that remains, however, is the range bias in radial direction for CryoSat-2. Envisat's data taken from [55] is corrected for this range bias.

The range bias represents the behavior of the satellite with respect to a reference level. [55] sets this reference to be TOPEX/Poseidon. While the correction for Envisat is well examined, the offset for CryoSat-2 SAR data is less known. [57] assesses the radial bias of CryoSat-2 with respect to Jason-2 based on the level-2 product (thus, the ESA retracker is used) using multiple crossover analysis. A spatial deviation in the range bias based on SAR is found, resulting in a SAR mean offset of 1.2 m with a precision of 15 cm according to [57]. However, this result needs to be considered carefully, as a radial offset (67.3 cm) and a time tag bias (0.5195 μs) in Baseline B [28] was not implemented in [57], however, it is taken into consideration within the data processing of this research. Therefore, the previously determined range bias is not applicable to the CryoSat-2 retracked data discussed here.

The reference offset provided in RADS has a magnitude of 2.6 cm [55], deviating significantly from the results provided by [57]. However, the reference offset in RADS is only based on LRM. It was shown in [57] that the radial range bias is significantly higher for SAR compared to LRM.

Within this research, the range bias provided by RADS is used. However, this value might be smaller as it is based on LRM data. A deviation from the used reference offset and the SAR reference offset can have a significant impact on the accuracy evaluation of retrackers. Consequently, it becomes apparent that more research in this range bias for SAR needs to be investigated in more detail, as it has an non negligible impact on the accuracy determination using crossover analysis.

The crossover analysis done using Envisat provides an impression of the general accuracy performance of retrackers, but fails to deliver more detailed results on which retracker does perform best. Therefore, the results presented in this section need to be considered carefully with respect to accuracy determination.

6-2-3 Results

As previously mentioned, the accuracy performance evaluation brings challenges along due to the scarce in-situ observations. The crossover analysis with Envisat showed that uncertainties remained in the accuracy performance. Therefore, the monthly mean of tide gauges is used to determine the retrackers' accuracy.

The mean sea level anomaly for the different waveform classes are shown in Figure 6-9. While the tide gauges are representative of ocean observations in coastal areas, it is difficult to find data that computes the accuracy for leads, sea ice or even unclassified waveforms. Therefore, only open ocean data is compared to the local observations of tide gauges. As the CryoSat-2 *SLA* values for the different retrackers are averaged over time (one month) and space (the test region), the temporal and spatial variability is minimized.

Figure 6-9 shows the mean sea level anomaly for three tide gauges in the ocean waveform. The tide gauge data differs per station, which is a result of the large distance between the tide gauges as was

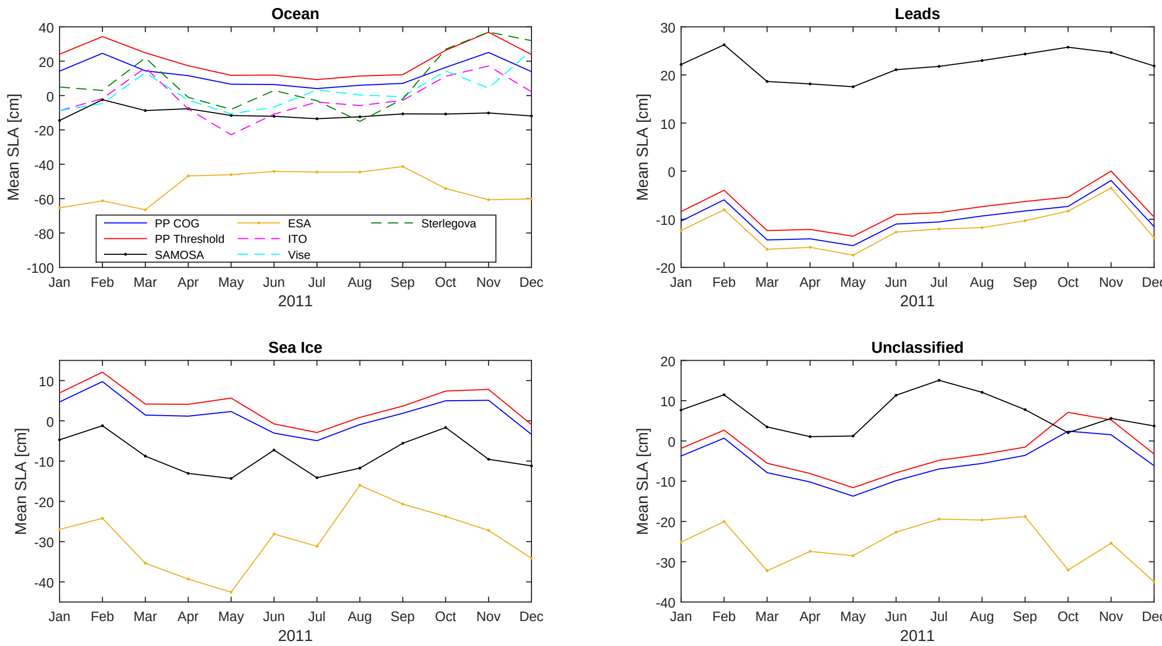

Figure 6-9: The *SLA* of different waveforms classes using the four retrackers for 2011. *Top left:* Ocean waveforms. The four CryoSat-2 retrackers are indicated by the solid lines. The tide gauge data of the three locations is shown in the dotted lines. *Top right:* Lead waveforms. *Bottom left:* Sea ice waveforms. *Bottom right:* Unclassified waveforms.

shown earlier. However, a similar seasonal tendency of all three gauges is visible which corresponds to the primary peak tendency.

For ocean observations, both primary peak retrackers as well as the SAMOSA retracker follow the same shape over the entire year at an offset. In the winter months, the sea level anomaly is higher for those retrackers than for the summer months. To further analyze the open ocean behavior of the retrackers with respect to the tide gauges, the difference between each retracker and the three tide gauges is computed. The mean of this difference is then shown in Figure 6-10. For a majority of the month, the SAMOSA retracker has the highest accuracy with respect to the mean difference of tide gauges. However, from October to December the primary peak retrackers outperform SAMOSA.

The seasonality that was discussed in Section 4-5, is visible for ocean observations, as for example in March and October until November, the performance of SAMOSA is worse compared to the primary peak Center of Gravity retracker (PP COG) as shown in Figure 6-10 with respect to the PP COG retracker. In all other months, SAMOSA behaves as the most accurate retracker for ocean observations.

Considering the leads track, all the empirical retracker are at a significant offset with respect to the physical SAMOSA retracker for all month. No clear explanation for this occurrence can be found, however, the cause is likely in the surface parameters of leads in the waveform. Furthermore, the range of *SLA* values is significantly smaller than for ocean. As there is no in-situ data for leads available, it is difficult to agree on which retracker performs the best and what effect a full analytic solution as implemented in SAMOSA on the waveform has.

The sea ice and unclassified data show that SAMOSA and the primary peak retrackers perform similarly with a given offset. The ESA retracker, however, returns *SLA* data that is at a significant distance with respect to the remaining retrackers. Furthermore, it should be noted that the threshold retracker,

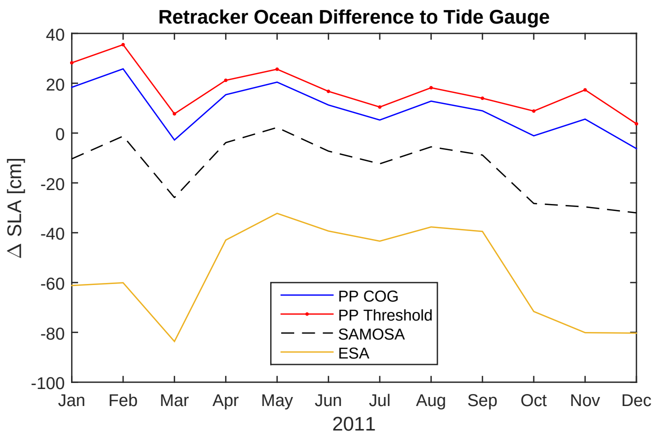

Figure 6-10: Difference in *SLA* computed over open ocean to the tide gauge data for the year 2011. The blue line shows PP COG, red represents the PP threshold, the black dotted line indicates SAMOSA and the ESA retracker is given in yellow.

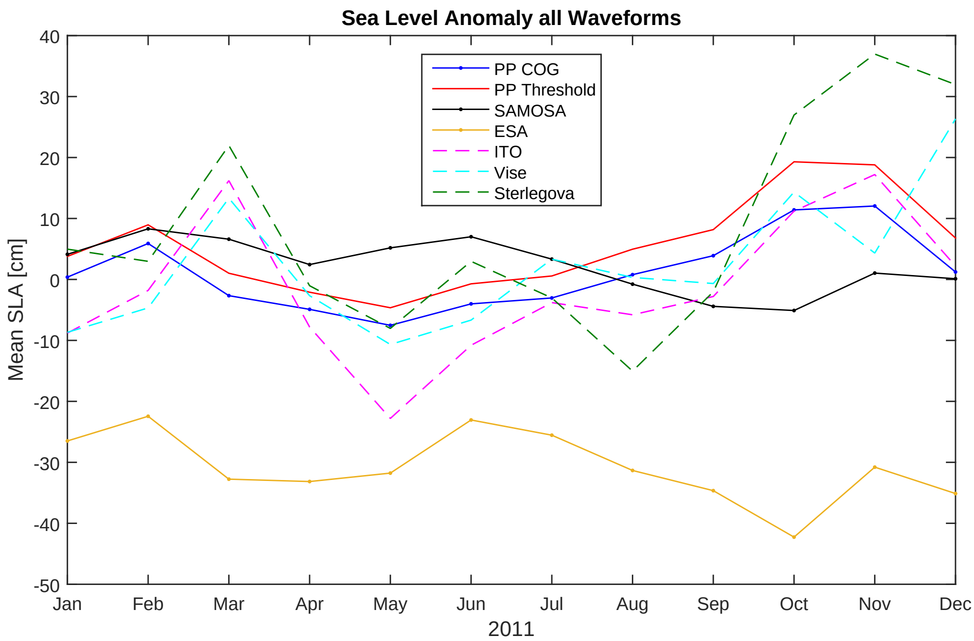

Figure 6-11: Mean sea level anomaly for the four retrackers (solid lines) and the three tide gauges (dotted lines) on a monthly basis for 2011. The waveform included in this plot are open ocean, leads and sea ice.

generally results in a slightly higher sea level anomaly value for all waveform classes compared to the primary peak COG retracker.

Ocean, leads and sea ice waveforms for the primary peak retrackers and SAMOSA follow the same shape throughout 2011 with respect to another, indicating that a bias remains within this data.

When combining, the ocean, leads and sea ice waveforms, the mean *SLA* per month is shown in Figure 6-11. For the sake of completeness, the tide gauge data are also indicated by the dotted lines. Generally, SAMOSA and ESA retracker show the same seasonal tendency that differs to the one of the primary peak retrackers. While SAMOSA and the primary peak retracker range in similar values as the tide gauge data, the ESA retracker differs significantly, showing that it performs the least accurate over the entire region.

The use of tide gauge data brings along some challenges. As the tide gauges are located in the coastal area in the SARIn mode mask and not over open ocean, they do not necessarily represent the absolute truth. Tide gauges represent the *SLA* at a spatial point over one month, which is compared to the mean of varying temporal and spatial observations of CryoSat-2.

Due to its high seasonality in the Arctic as was discussed in Section 4-5, the *SLA* differs significantly over the test region, meaning that the conditions at another point in the test region might be deviating to the ones shown by the tide gauge.

When analyzing Figure 6-9 to Figure 6-11, one element that is left in the tide gauge and retracker *SLA* data is the annual signal. The annual signal has a period, f_{ANN}, of one year and has a changing magnitude within this year which affects the sea level anomaly. The annual signal, h_{ANN}, is computed using Eq. (6-4), with A_{ANN} and ϕ_{ANN} representing the amplitude and phase of the signal respectively.

$$h_{ANN} = A_{ANN} \cos\left(2\pi f_{ANN} t - \varphi_{ANN}\right) \tag{6-4}$$

Significant spatial variation in the magnitude is present in the annual signal. Figure 6-12 shows the amplitude and phase over the test region based on Denmarks Tekniske Universitet (DTU)13 annual tide model which has a resolution of 1° x 1° [53]. A clear spatial deviation in both amplitude and phase can be observed that affects the representative meaning of tide gauges for the test region. Throughout the test region over a period of one year, the difference in annual signal varies from a minimum of 2.9 cm to a maximum of 9 cm.

Therefore, computing the accuracy of retrackers based on tide gauge data lead to a remaining uncertainty. As was observed in Figure 6-9, the tide gauge data is positioned in between the primary peak

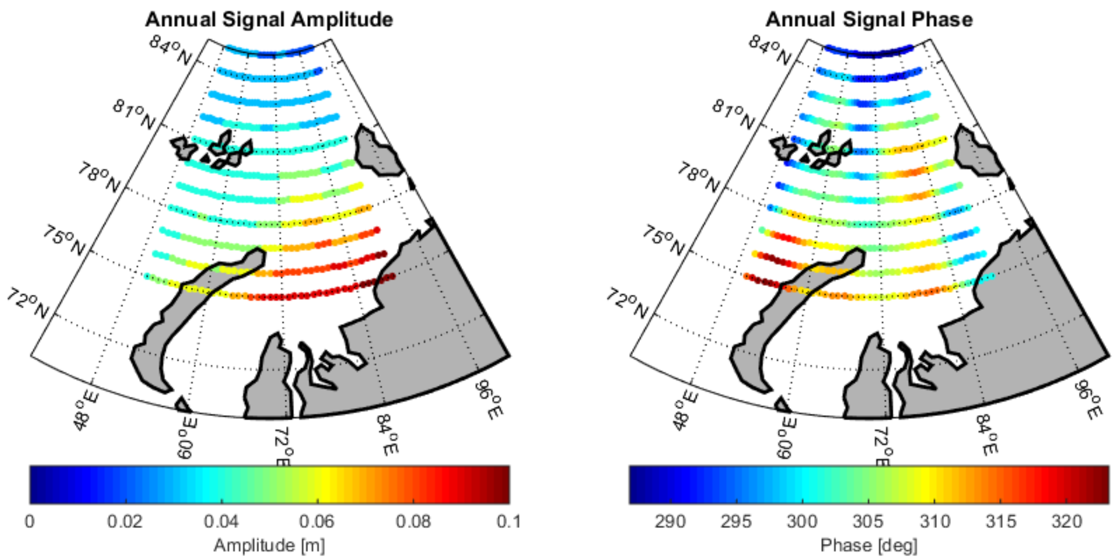

Figure 6-12: The annual signal in the test region based on DTU13 1°x1° resolution [36]. *Left:* The amplitude of the annual signal. *Right:* The phase of the annual signal.

retrackers and SAMOSA. However, with an offset of up to 9 cm, the retracker selection for ocean can be affected.

It can be concluded that a decision on accuracy needs to be considered carefully due to large remaining uncertainties. First of all, the radial bias in the CryoSat-2 data needs to be determined in more detail for SAR observations making a crossover analysis with other radar altimeters at this moment unreliable. Furthermore, tide gauge data provides significant spatial limitations for this research.

6-3 Optimal Retracker Selection

The optimal retracker is selected by combining the results of the precision and accuracy performance per waveform class and month. For ocean waveforms, the decisive factor was the accuracy behavior of the sea level anomaly, while for leads and sea ice waveforms, precision was dominating. The reason for this different evaluation of retrackers was the lack of accuracy reference data for leads and sea ice.

As was shown before, the sea ice precision performance for SAMOSA was very high during summer months, due to the lower number of observations. In order to avoid a false assignment of a retracker, the number of observations are taken into consideration during the selection as well. As was shown for sea ice data in summer months, only few SAMOSA and ESA retracker observations exist, due to the strong a priori filter requirements. Consequently, the threshold retracker was selected for sea ice as it performs best by including the largest data set (during July to September). Table 6-2 provides an overview of the selected retrackers that will be used in the following to implement a retracker system with an appropriate bias removal strategy.

It should be noted that there is no clear seasonal dependency per waveform class in the best retracker selection for leads and sea ice. The ocean waveform classes are best retracked for the majority of the months using SAMOSA, however, in the winter months (October to December), the primary peak retracker outperform SAMOSA.

A retracker whose performance was not discussed in this chapter is SAMOSA2. As was explained in Section 5-2, SAMOSA2 includes more terms of the Bessel function in its analytic solution. It was

Table 6-2: Selected retracker per month per waveform class. The ocean retrackers are selected based on accuracy, while leads and sea ice waveforms are chosen based on precision performance.

	Ocean	**Leads**	**Sea Ice**
January	SAMOSA	COG	Threshold
February	SAMOSA	Threshold	Threshold
March	COG	COG	Threshold
April	SAMOSA	COG	Threshold
May	SAMOSA	COG	Threshold
June	SAMOSA	COG	COG
July	COG	COG	Threshold
August	SAMOSA	COG	Threshold
September	SAMOSA	COG	Threshold
October	COG	COG	COG
November	COG	COG	Threshold
December	Threshold	COG	Threshold

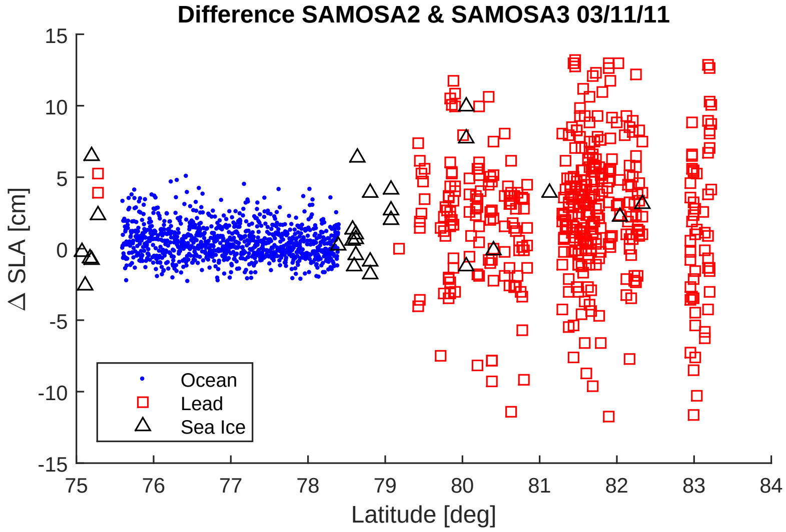

Figure 6-13: The difference in *SLA* between SAMOSA2 and SAMOSA3. The ocean observations of SAMOSA3 are blue dots, leads are red squares and sea ice is shown by black triangles.

decided to use SAMOSA3 instead of SAMOSA2, due to its lower computation time. Nevertheless, a comparison with respect to its accuracy and precision was made. Figure 6-13 shows the difference in terms of *SLA* for one track in the beginning of November (03/11/2011). For ocean waveforms (blue), the difference between the two retrackers is small and does not exceed 5 cm. However, the difference for leads and sea ice (red and black respectively) results in a larger spread of up to 14 cm. For ocean observations, the change in *SLA* values has a small effect on accurady, when comparing it to the tide gauge data (see Figure 6-8). The effect on accuracy performance is difficult to assess for leads and sea ice, as validation data is scarce.

A similar observation was found for the precision performance of SAMOSA2. A small difference concerning the ocean performance was found, while the difference for irregular waveforms was significantly higher. However, the robust and fast computation of sea level anomaly for SAMOSA3 [58] is the decisive advantage over SAMOSA2. For more information on the performance determination of SAMOSA2, the reader is referred to Appendix B.

Chapter 7

Retracker System

When developing a year round retracker system one major challenge is offset removal. The origin of this bias lies in the algorithm since it is not able to cope with noise present in the retracked waveform. As was described in Chapter 5, the working principle of the four retrackers assessed in this research varies significantly from empirical to physical retrackers. Therefore, an offset in sea level anomaly is expected to occur when a surface point is retracked by two different algorithms.

To remove this offset in the year-round retracker system, different bias removal strategies are developed and analyzed based on their accuracy and precision performance. Finally, a verification of the developed bias removal strategies is executed.

7-1 Bias Removal Strategies

Two assumptions are used in the development of the bias removal strategy. For the first strategy, the mean difference bias, it is assumed that the mean offset over open ocean is representative for the mean lead and sea ice offset. The second strategy, assumes that for every waveform class a dependency on significant wave height, *SWH*, can be created. In the following the two strategies and the implication of these assumptions are explained and discussed in more detail.

7-1-1 Mean Difference Bias

The mean difference bias, here after only called mean bias, computes the difference in sea level anomaly, *SLA*, of two different retrackers over open ocean per track. This mean difference is then used to adjust other waveform classes (leads and sea ice) in the track. Open ocean waveforms are used in this approach due to their predictable and regular waveform [59].

The mean bias method is a simplistic approach that corrects the retracker offset to certain extent. However, it does not take noise in irregular waveforms (caused by sea ice for example) into consideration, which leads to a remaining bias between two retrackers.

As was elaborated on in Section 6-3, the ESA retracker was discarded due to its poor accuracy and precision performance. Since three different retrackers are used within the developed year round retracking system for the Arctic, the mean differences are computed with respect to a selected base retracker. Two retrackers are selected to serve as a base retracker: Primary peak COG retracker and SAMOSA. The primary peak retracker is chosen as it is able to retrack all waveform classes while providing a maximum number of data points. Furthermore, the waveform is not affected by noise in the trailing edge, resulting in an estimation of solely the algorithm offset.

Secondly, SAMOSA is selected as a base retracker due to its good performance in ocean waveforms and therefore good prediction capabilities of the systematic bias in the algorithm with respect to another retracker.

When considering the mean offset for ocean and comparing it to leads and sea ice, it can be observed that the sign of the ocean offset is not necessarily equal to the sign of leads or sea ice. In order to avoid falsely adding an offset where it should be subtracted, attention is paid to adjusting the offset such that the offset between two retrackers is reduced in any case.

7-1-2 SWH Dependency Bias

Literature showed that the offset between two retrackers for conventional altimetry is a function of significant wave height, *SWH* [59] and was applied for the first time to SAR technology by [30].

Generally, the *SWH* dependent offset changes per track, meaning that there is no unique equation describing all scenarios. Similar to the mean bias offset, the parameters of the offset equation need to be determined per track for every waveform class. However, it should be noted that for sea ice observations as well as leads, *SWH* dependency needs to be considered carefully, due to scarce data.

[30] showed that a linear relation of the offset as a function of *SWH* can be applied to remove the combined offset as described by Eq. (7-1), where α and β represent coefficients that are computed per track.

$$\text{Offset} = \alpha + \beta SWH \tag{7-1}$$

In this method a least squares approach is applied as shown in Eq. (7-2). Here, b represents the bias between two retrackers and A is the design matrix providing the elements of the function that is used to remove the bias. The coefficients of the parameters described in the design matrix are expressed by x and the residuals are represented by ε. The aim is to find a solution to the least squares which minimizes the normalized residuals, $\varepsilon^T\varepsilon$. Eq. (7-3) shows a solution for the best estimate of the coefficients for a fully ranked matrix. The rank of a matrix indicates the size of a subset matrix that is nonsingular [7]. Based on this solution, the residuals are then determined using (7-4). Data points whose standard deviation of the residual is larger than 2.5 times the standard deviation of all residuals are removed.

$$\boldsymbol{b} = A\boldsymbol{x} + \boldsymbol{\varepsilon} \tag{7-2}$$

$$\hat{\boldsymbol{x}} = \left(A^T A\right)^{-1} A^T \boldsymbol{b} \tag{7-3}$$

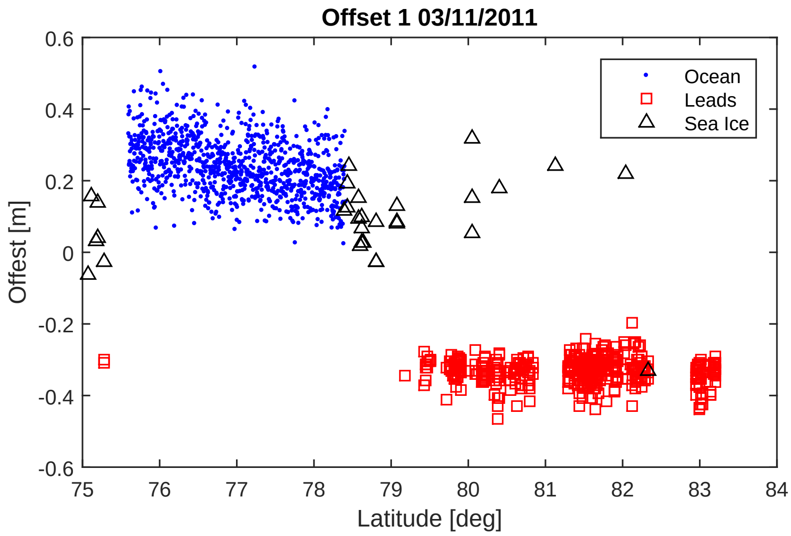

Figure 7-1: The offset between PP COG and SAMOSA retracker for a track on November 3, 2011. Ocean observations are indicated by blue dots, red squares show leads and sea ice is presented by black triangles.

$$\hat{\boldsymbol{\varepsilon}} = \boldsymbol{y} - A\hat{\boldsymbol{x}} \tag{7-4}$$

In order to find the optimum offset removal approach, the same two tracks in July and November are considered that were discussed previously in Chapter 6.

The offset between the primary peak COG and SAMOSA is computed for each waveform class separately in order to account for their different behavior. No unclassified waveforms are taken into account here as their behavior is unpredictable. Figure 7-1 shows that the offset of the three waveform classes are in two different ranges. Furthermore, it can be seen that ocean offsets between two retrackers have a higher variability compared to lead offsets. A reason for this deviation could be that leads are better retracked due to all their power being in the primary peak. Therefore, the waveforms of leads are able to be well retracked by both empirical and physical retracker. Ocean waveforms on the other hand have a more diffused waveform and therefore, the estimation of the retracking point can differ significantly for the empirical and physical retrackers. This results consequently in a larger spread of the offset values.

Different parameter combinations are analyzed in order to find the most efficient offset removal strategy. Table 7-1 shows the normalized residuals for a number of different offset dependent removals for open ocean. The same pattern is observed for other waveforms. However, for sea ice and leads observation, it was not possible to provide a result for functions that include the wind speed. This could be due to the wind speed data provided by SAMOSA. Table 7-1 shows that an offset removal strategy as a function of wind speed and backscatter coefficient provides the largest normalized residuals. The reason for this is that the wind speed is a function of backscatter, meaning that only one independent variable is used. Therefore, this strategy is discarded.

The data on *SWH*, backscatter, σ, and wind speed at an altitude of 10 m above the surface, u_{10}, is provided by SAMOSA [18]. However, strong filtering applies to this data which results in significantly less data points of these parameters compared to the number of primary peak retrackers data points.

Table 7-1: Normalized residuals for two different offsets for ocean waveforms for two tracks in the beginning of July and the beginning of November. *Offset 1* represents the difference between PP COG and SAMOSA. *Offset 2* is the bias between PP Threshold retracker and SAMOSA.

Ocean	**Offset 1 normalized residuals**		**Offset 2 normalized residuals**	
	03/11/11	01/07/11	03/11/2011	01/07/2011
f(SWH)	0.878	2.554	1.622	4.147
f(SWH,u_{10})	0.878	2.568	1.594	3.878
f(SWH,σ)	0.878	2.575	1.596	3.919
f(SWH,u_{10},σ)	0.877	2.510	1.575	3.902
f(u,σ)	2.821	3.834	4.291	5.953
f(SWH,SWH^2)	0.851	2.513	1.583	4.169
f(SWH,SWH^2,SWH$\cdot u_{10}$)	0.851	2.542	1.600	3.922
f(SWH,SWH^2,$u_{10}\cdot$ SWH, $u_{10}^2\cdot$ SWH)	0.829	2.532	1.585	3.922

The SAMOSA data is preferred for the geophysical parameters over the ESA Level-2 data, as the Level-2 data was very scarce and unreliable for the test region.

Generally, the offsets in July and November have a similar pattern. The last row of Table 7-1 indicates the parameters that are used to compute the sea state bias based on the four parameter model (BM4). This function together with the function of *SWH* and SWH^2 perform the best as their normalized residuals are very similar. It is expected that the sea state bias equation performs very well as it is used over open ocean, however, for leads, no wind speed was determined, resulting in an insufficient strategy. Thus, the bias removal strategy which is a parabolic function of both *SWH* and SWH^2 is selected in this research. This bias removal method outperforms the linear dependent *SWH* strategy as discussed in other literature for both offsets in November and has only for the July track slightly higher normalized residuals. Figure 7-2 shows the bias of SAMOSA and PP COG retrackers as a function of *SWH* for the November track, as well as the selected bias equation. It can be observed that the fitted offset equation fits the data well for ocean observations.

Using these results, the design matrix, *A*, of size n x 3, is determined as shown in Eq. (7-5). The n x 1 bias vector, *b*, is given by Eq. (7-6) and *n* represents the number of valid data points for a given track. By inserting these equations back into Eq. (7-3), the least squares solution of the 3 x 1 coefficient vector is determined. A least squares solution can only be obtained when m $\geq$ 3, which is the number of columns of the design matrix, as it is otherwise rank deficient.

$$A = \begin{bmatrix} SWH_1^2 & SWH_1 & 1 \\ SWH_2^2 & SWH_2 & 1 \\ \vdots & \vdots & \vdots \\ SWH_n^2 & SWH_n & 1 \end{bmatrix} \tag{7-5}$$

$$b = \begin{bmatrix} b_1 \\ b_2 \\ \vdots \\ b_n \end{bmatrix} \tag{7-6}$$

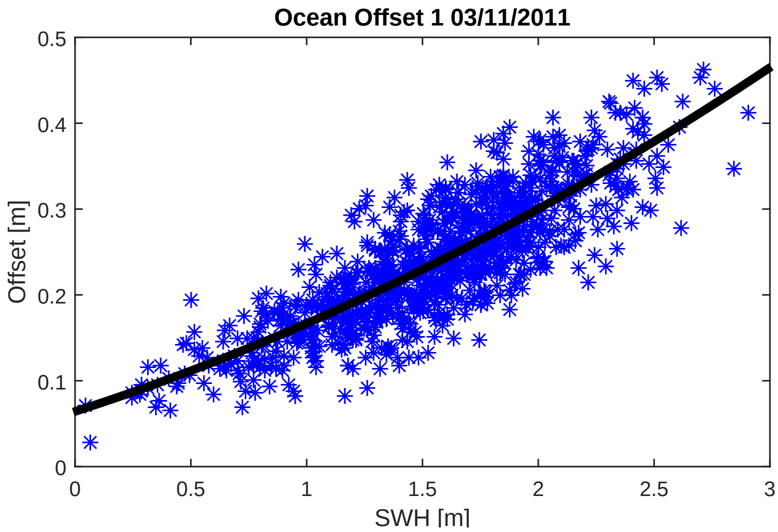

Figure 7-2: Offset between PP COG and SAMOSA of the November track as a function of *SWH* (blue). The bias removal is shown in black. It is a function of *SWH* and SWH^2.

If the number of rows in the design matrix does not exceed the number of columns, thus m < 3, then the minimum norm solution is used. Here, the design matrix has a rank lower than 3. The minimum norm solution aims to minimize the sum of squares of the residuals [7]. The solution obtained using this method is then expressed by Eq. (7-7).

$$\hat{\boldsymbol{x}} = A^T \left(A^T A\right)^{-1} \boldsymbol{b} \tag{7-7}$$

7-1-3 Hybrid Model

One limitation of the SWH dependent model is the scarce data of significant wave height in the Arctic region. Therefore, the performance of the bias removal strategy strongly depends on the availability of the *SWH*. As has been mentioned before, significantly less data is available for leads and sea ice. In order to improve the quality of the bias removal strategy two hybrid models of the two original methods is developed.

The ocean offset can be well modeled using the *SWH* method as sufficient data points are available. While for leads also *SWH* data is present, the sea ice waveforms have only very few data points. Table 7-2 shows that this hybrid model uses the *SWH* model for ocean observation and the mean bias removal strategy for leads and sea ice.

Table 7-2: An overview of the bias removal methods used in the hybrid model.

	Ocean	**Leads**	**Sea Ice**
Hybrid Model	SWH	Mean bias	Mean bias
Hybrid Model V2	SWH	SWH	Mean bias

7-1-4 Hybrid Model V.2

The second hybrid model uses for ocean and leads offset determination the *SWH* model. The sea ice offset is removed using the mean bias strategy as indicated in Table 7-2. Using this model it is interesting to compare the number of *SWH* observations for leads, as this is the only change between the two models. By considering the number of observations used to compute the model, the data set is assessed. Both hybrid models will be implemented and tested for their performance.

7-2 Verification

The software for the two main bias removal strategies based on *SWH* bias and mean difference are developed during this thesis. In order to prove the well functioning of this software, it is verified as shown in Table 7-3. The expected output is equal to the actual output for all strategies.

Considering the mean difference method, two normally distributed random data sets of sea level anomaly are created with the second one being at an arbitrarily selected offset to the first one. The mean bias software computes the offset over 10,000 runs, the determined offset is then averaged to find the deviation of the a priori selected offset and the computed bias. The result for an a priori set bias of 10 cm is shown in Figure 7-3, the two values deviate of 0.07%. Thus, the mean bias software is indeed well functioning.

The *SWH* bias removal strategy is verified using two different approaches. The first assumes that the offset between the two sea level anomaly data sets that are created is constant. Thus, the *SWH* is zero, resulting in a rank insufficient design matrix. During the second verification approach, a priori the least squares coefficients are determined on which the two data set are based. Using the *SWH* bias removal software, the coefficients of the least square are computed. It is expected that the computed coefficients are then equal to the a priori set values. Both methods show that the designed software behaves as expected.

Table 7-3: The verification procedure of the two developed software

	Input	**Expected Output**
Mean difference	- Two data sets with a constant offset - Compute offset parameter of the two data sets	- Computed offset through the bias method is equal to input offset
SWH bias	- Two data sets with zero *SWH*, thus constant offset - Compute the design matrix of the two data sets	- Design Matrix is rank insufficient and has a rank of one
	- Two data set with offset determined by coefficient values - Determine the offset coefficients	- Computed least squares coefficient are equal to a priori values

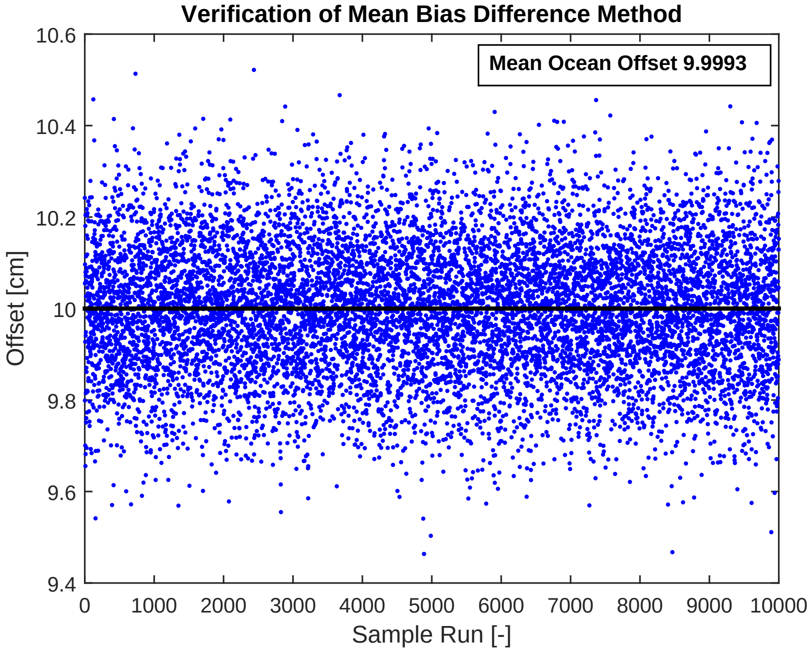

Figure 7-3: Verification of the mean bias difference method. The black line shows the a priori set offset in the two data sets. The blue line indicates per run the computed offset by the algorithm.

7-3 Results

Based on the selected retrackers per waveform class that were described in Section 6-3, the accuracy and precision of this retracking system can be determined. In order to remove the bias caused by the use of different retracking algorithms, the bias removal strategies of Section 7-1 are applied.

In the following section, first the processing of the combined retracker system is elaborated, then the precision and accuracy of the retracker system is assessed. Finally, the effect of the bias removal system is discussed.

7-3-1 Retracker System Processing

Due to the combination of differently retracked data, a filter is applied to the sea level anomaly, *SLA*, in order to remove outliers. The reason to apply a filter is that for example when using the mean bias removal strategy, the offset over open ocean is applied to the *SLA* of leads and sea ice. As the offset over open ocean can be well determined due to the predictability of the waveform, it is simpler and may vary in magnitude compared to the offsets of complex waveforms like leads and sea ice. Therefore, random noise is introduced into the *SLA* for leads and sea ice.

Another reason to implement a filter is the error that remains after the *SWH* dependent offset removal strategy is applied. The *SWH* dependent offset removal strategy aims to minimize the normalized residuals of the least squares solution. To minimize the remaining error in the retracker system, outliers in the sea level anomaly data are determined and accounted for using a filter.

The applied filter is a Hampel filter as explained in [60]. The Hampel filter uses a moving window that is centered at one data point and includes 3 data points on each side of the center data point. The center data point is considered an outlier, if its value exceeds three times the standard deviation of the moving window. In case the data point is marked as an outlier, it is replaced by the median value of the window. This process is repeated for all sea level anomaly data in one track.

The along-track resolution of CryoSat's 20 Hz data that is used in this research is 278 m [6]. A Hampel filter with a moving window of in total seven measurements is applied (three on each side of the center data point additional to the center data point). Thus, the along-track distance over which the moving window stretches is in the ideal case 1.67 km (6·278m). If there are data points missing, due to for example strong filtering, the along-track distance of the moving window of the filter is slightly larger. As only small variations in the sea level anomaly over such a distance is expected, the size of the moving window is sensible while not allowing a large remaining error in the data.

7-3-2 Precision

The precision of the retracker system is assessed using the 1 Hz standard deviation of the sea level anomaly. Since the retracker system is a combination of selected retrackers based on their behavior for different waveform classes, a bias is inserted in the data when combining them (the selected retrackers are found in Table 6-2). The performance of the retracking system with the bias removal strategies implemented provides an insight on the performance of the various strategies.

Standard Deviation

As a first step in the precision performance analysis, the standard deviation per month for ocean, leads and sea ice is computed as shown in Figure 7-4. Besides the standard deviation of the retracking system with five bias removal strategies, also the primary peak center of gravity (PP COG) and SAMOSA retracker are shown as a reference.

Starting with the mean bias removal strategy that has SAMOSA as a base retracker (in the figure indicated as Mean Bias SAMOSA, hereafter MBS), it performs better than the SAMOSA retracker

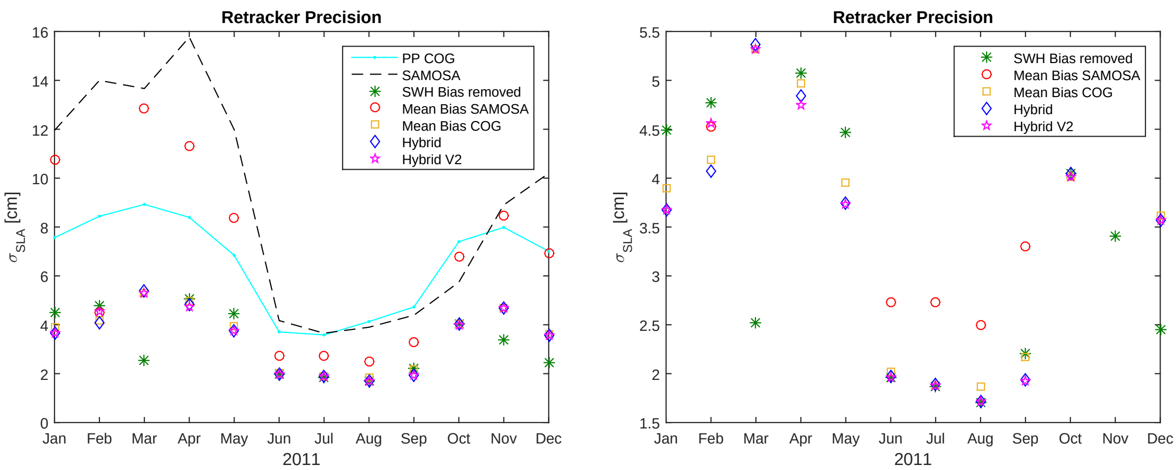

Figure 7-4: Precision of the retracker system using different bias removal strategies. *Left:* The standard deviation of the bias removal strategies as well as SAMOSA and PP COG are shown. *Right:* A close-up of the standard deviation value for the different bias removal strategies.

for all months except October. In October, all waveform classes are retracked using the PP Center of Gravity (COG) retracker. One explanation for this behavior can be that the offset for ocean between SAMOSA and PP COG is too scattered. Therefore, the mean difference over open ocean is not representative of the difference for irregular waveforms such as leads and sea ice.

An extreme seasonal tendency can be observed for MBS, with lower standard deviations in the summer (June to September) compared to the winter months. This tendency is directly related to the percentage of sea ice waveforms as indicated in Figure 4-7. The lower standard deviation in summer is a consequence of the lower sea ice observations, thus the impact of adjusted sea ice waveforms is smaller. Previously, it was shown that the mean sea ice offset is more volatile than the open ocean offset. By having fewer sea ice observations, less variability is left in the data as the remaining waveform classes are well predicted and adjusted for.

Notable is also the dip in the standard deviation of MBS in February, resulting in a similar level as the mean bias method using the PP COG (short MBC) retracker as a basis. The reason for this could be that the mean ocean offset is less volatile due to the fewer ocean observations. Therefore, a better fit of the sea ice and lead offset is created resulting in a significantly lower standard deviation.

The other bias removal strategies have a similar seasonal tendency as MBS, however less extreme. The reason for this lies with the base retracker choice. Since most ocean waveforms are retracked using SAMOSA, the ocean offset is well corrected in MBC. Furthermore, except February, all leads are retracked using PP COG, meaning that no adjustment for this waveform class is necessary. The sea ice waveform are retracked using either of the primary peak retrackers which behave very similar. Thus, overall the offset with respect to the base retracker of PP COG is more predictable than for a SAMOSA base retracker. Generally, MBC behaves significantly better over the entire year than the original primary peak COG retracker and the MBS.

The second bias removal strategy is based on *SWH* and hereafter referred to as SWHB. It uses the PP COG retracker as a base retracker, since this retracker has more data point observations compared to SAMOSA.

Generally, the behavior of SWHB is similar to MBS, however, during March, November and December the lowest standard deviation is reached with SWHB. This is due to the number of points that are retracked in these months. Figure 7-5 shows the ratio of data points used in the retracker system with removed bias to the total number of data points of the base retracker in the track. In March, November and December, fewer data is available as the SWHB only considers data points if there is a *SWH* data available that is not smaller than -0.5 m. In March, November and December, open ocean is retracked using either of the primary peak retrackers. However, there are significantly less tracks of Baseline B SAMOSA data provided by GPOD [18] with respect to the number of tracks of the primary peak retrackers. Due to the lower number of data points, the variability in these months is lower compared to other months.

Both hybrid models behave very similar to each other with respect to precision. This is to be expected since the leads waveform bias removal is the only difference in the strategies. In June, a month with a high number of lead observations hybrid model V2 (hereafter HB2), has a slightly better precision than hybrid model (hereafter HB1). Generally, both models differ not significantly from another in terms of precision. However, when considering the number of data points, it is observed that in particularly in December, the hybrid models include a lower number of points than MBC, while providing a similar level of precision.

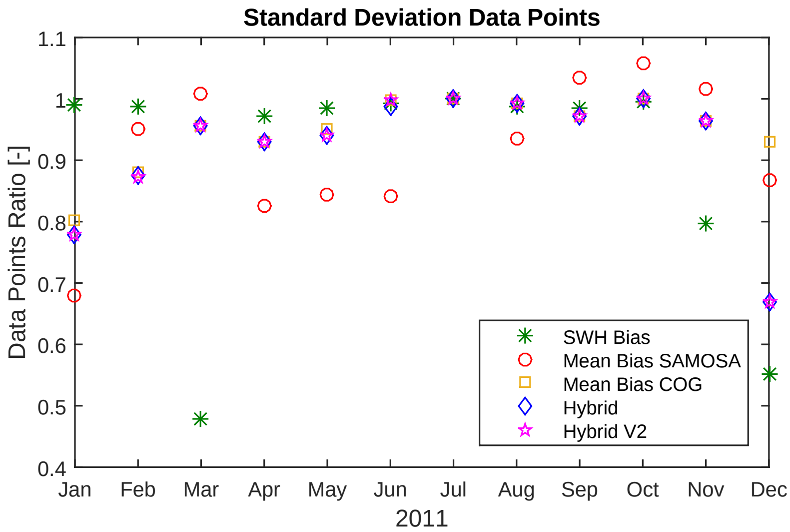

Figure 7-5: The data point ratio computed for the standard deviation is shown for the five different bias removal strategies. The ratio is computed as the number of observations used in the retracker system over the number of points used in the base retracker.

Improvement Coefficient

In order to assess the change in precision of the retracker system, the improvement coefficient, *IMP*, is introduced. Eq. (7-8) computes this parameter similarly to the description in [59]. The standard deviation of the base retracker and the retracker system is given by σ_{base} and σ_{comb}, respectively.

$$\mathrm{IMP} = \frac{\sigma_{\mathrm{base}} - \sigma_{\mathrm{comb}}}{\sigma_{\mathrm{base}}} \cdot 100\% \tag{7-8}$$

Figure 7-6 shows the improvement coefficient for the five bias removal strategies. MBS is the only improvement coefficient that is computed with respect to SAMOSA, the remaining bias removal strategies use PP COG as a reference retracker. The negative value for MBS in October reflects the result found in the standard deviation figure that the precision is lower for the retracker system compared to the base retracker.

MBS has the smallest improvement compared to the remaining strategies. The reason why MBS performs lowest for the large majority of the months is that irregular waveforms (leads and sea ice) are not retracked using SAMOSA but one of the primary peak retrackers. The offset of sea ice and leads contains more noise than the ocean offset which introduces another offset that cannot be compensated by this strategy.

The *IMP* of MBS for February is significantly higher compared to other retrackers. As the data point ratio (see Figure 7-5) is close to one, it leads to the reason that MBS is well modeled for the threshold retracker and only small variations are present in the mean offset value of the different waveform classes.

The improvement coefficient of SWHB shows a similar behavior as the standard deviation. The highest improvement coefficient is reached in March, November and December by SWHB due to the low number of observations in that period. Significantly less data points are taken into consideration in

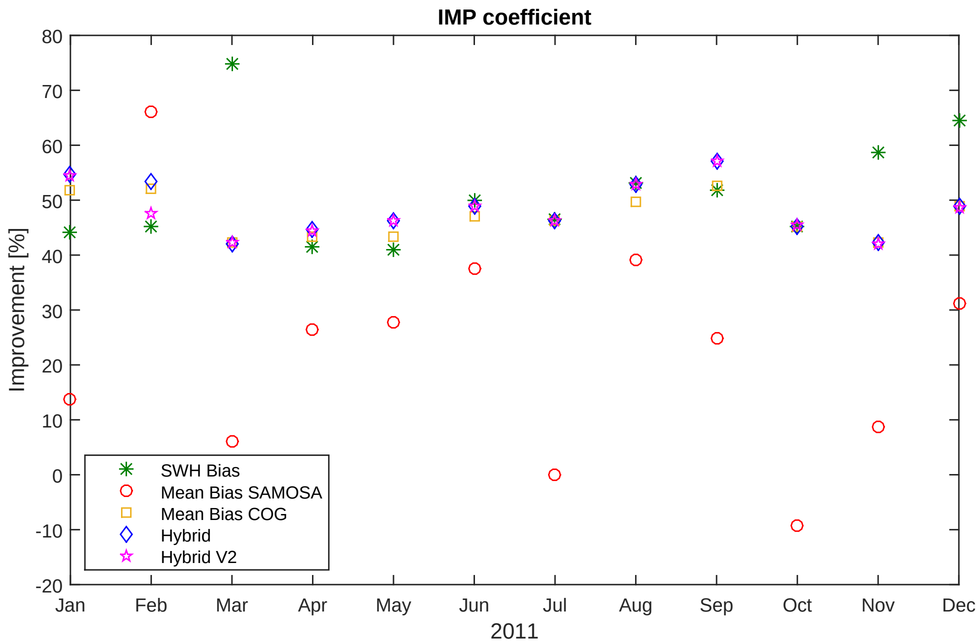

Figure 7-6: Improvement coefficient for the retracker system using five different bias removal strategies.

those months due to the small number of SWH data provided by SAMOSA. This shows the limitations of the SWH bias removal strategy for the high latitudes.

The retracker system using the Mean Bias COG removal, MBC, performs well throughout the entire year while including a large number of data in the analysis. In months with high leads and sea ice waveforms, MBC and both hybrid models, perform the best as they have a low standard deviation and a high improvement coefficient while obtaining a high ratio of data points.

The hybrid models perform very close to another and to MBC. Table 7-4 shows the mean standard deviation, mean improvement coefficient and the mean data point ratio for the year 2011 in the Kara Sea. The lowest values are reached by SWHB, however, they are not representative due to the low number of data points. The hybrid models as well as MBC perform in all categories very closely together. As the hybrid models have months where less than 80% of the data are included, the precision of the retracker system using MBC is selected to perform best. A high data point ratio is selected as a decisive criterion, as it provides a complete overview of the varying conditions that are measured in the Arctic. If the data point ratio is low, this might affect the precision and accuracy behavior.

Table 7-4: The mean standard deviation an mean improvement coefficient per retracker system with different bias removal method for 2011.

	MBC	**MBS**	**SWHB**	**HB1**	**HB2**
Mean σ [cm]	3.55	6.78	3.25	3.46	3.48
Mean IMP [%]	47.1	22.7	51.3	48.5	48.1
Mean Data point ratio [-]	0.948	0.915	0.894	0.922	0.923

7-3-3 Accuracy

The accuracy of the retracker system is determined with respect to reference data. In this case tide gauge data is used (for an explanation on the data handling of tide gauges, the reader is referred to Section 6-2-1).

The left side of Figure 7-7 shows the sea level anomaly for the retracking system using different bias removal system. The same seasonal tendency can be observed for all retrackers which have the PP COG as a base retracker, while significant differences can be observed to the retracker system using Mean Bias SAMOSA, MBS, for bias removal. In particularly in the winter months (August - February) a significant deviation of MBS with respect to the Mean Bias COG, MBC, can be observed. This is caused by the large number of leads and sea ice observations which are not well modeled by the ocean offset of SAMOSA.

The large number of leads and sea ice observations that are retracked by the primary peak retrackers result in an increase in data points in the MBS retracker system. Therefore, more data points are implemented in the retracker system compared to the SAMOSA base retracker. Consequently, a data point ratio of larger than one is reached in September and October as shown on the right in Figure 7-7.

Figure 7-7 indicates that MBS deviates further from the zero *SLA* throughout the year, due to the higher volatility of irregular waveform offsets with respect to ocean offsets.

The remaining retracker systems behave very similar for the entire year with respect to their sea level anomaly values. Comparing this to the data point ratio, it is seen that the significant wave height bias, SWHB, provides the highest ratio for a majority of the months. Furthermore, the hybrid models and MBC have similar data points ratio in all month except November and December which could be caused by the lower number of available *SWH* data that is needed for the bias removal of ocean waveforms. MBC provides a high ratio of data points throughout the year and is the only retracker with a ratio of above 80% for the entire year of 2011.

When comparing the sea level anomaly to tide gauge data, all waveform classes are taken into consideration as the overall performance is assessed. If only the ocean waveforms would be analyzed a

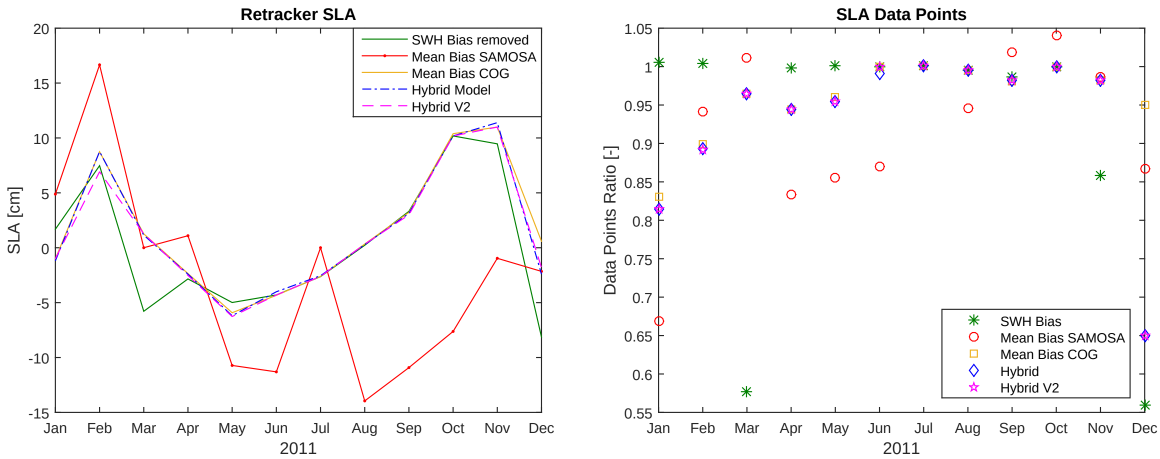

Figure 7-7: The sea level anomaly performance for a retracking system based on different bias removal strategies. *Left:* The sea level anomaly for 2011 is shown. *Right:* The data point ratio is computed by taking the ratio of data points included in the retracking system over the total data points of the base retracker.

similar result as the one described in Section 6-2-1 is expected, as the accuracy of the overall retracking system has changed and not the one of the individual waveform classes.

By using all waveform classes, limitations in the meaning of accuracy analysis are reached, as in particular in winter months (January to April), sea ice is the dominating waveform class. Tide gauge observations are not representative for sea ice or leads waveforms.

The difference between each retracking system and the three tide gauges is computed. The mean of this difference per month is then plotted in Figure 7-8. Both hybrid models and MBC have a similar accuracy behavior over the entire year with only small deviations from another. The deviations between the hybrid models are in particular in May and June visible. These are two months with a high number of lead waveforms.

The accuracy of the combined retracker strongly depends on the base retracker choice as seen when comparing the retracker systems using a MBS and MBC approach to another. A significant offset in ΔSLA can be observed between those retrackers, meaning that an offset is present in the retrackers.

MBC only slightly deviates from the ΔSLA of the pure PP COG retracker and outperform for most months the accuracy of the pure SAMOSA retracker. However, it seems that in May, the accuracy with respect to tide gauges has decreased using the hybrid models and MBC when comparing it to COG retracker. The reason for this is that the ocean values are adjusted to fit the PP COG retracker which performs less accurate in this waveform class. Therefore, the offset between retrackers is removed in SLA, however, adjusted to a wrong reference.

This accuracy analysis should be considered carefully, as an accuracy assessment based on tide gauge data is not fully representative. Here, sea level anomaly data of all retrackers over a test region are compared with three points within the region. Thus, the same issues of annual signal, mode mask and waveform differentiation that were described in Chapter 6 are applicable. Therefore, tide gauge data

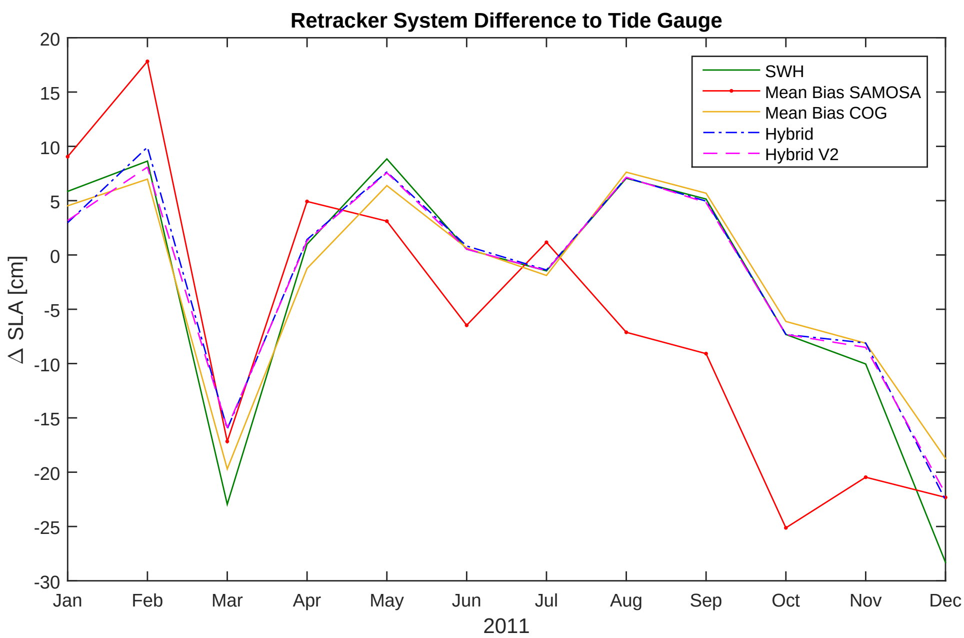

Figure 7-8: The difference in sea level anomaly of each retracking system with respect to the three tide gauges is computed. The mean of this value is shown for the five bias removal strategies.

cannot be seen as the absolute truth but rather gives a general indication of accuracy performance.

As it is generally difficult to find suitable in-situ observations at these high latitudes, a recommendation is to consider another test region that includes tide gauges that are in SAR mode. There are two potential tide gauges that meet this requirements: Ny-Alesund in the coastal area of Svalbard and a tide gauge on Novaya Zemlya. However, both tide gauges do not provide a good solution to the issue as Ny-Alesund's performance is insufficient and the tide gauge on Novaya Zemlya can only be used during summer months [private communication, Ole B. Andersen 2016].

A crossover analysis as done previously, is not valuable for the accuracy assessment of the retracker system as the crossover analysis provided insight into the performance of an individual waveform class - ocean waveforms.

Based on the accuracy and the precision performance, MBC is selected as the optimal bias removal strategy. In particular for the precision performance, MBC performs well by including a constantly high number of data per month. Concerning its accuracy, it is difficult to determine how it behaves, however, also here a high data ratio is included in the computation of the monthly sea level anomaly.

Figure 7-9 shows the mean standard deviation of the test region in February and June at the top and bottom, respectively. These two month have been selected since February contains a high number of sea ice observations, while having a low number of open ocean and June has a high number of leads with low sea ice. Furthermore, in February, ocean waveforms are retracked using SAMOSA, while sea ice and lead waveforms are retracked with the threshold retracker. Therefore, the effect of the bias removal strategy becomes visible.

On the left side of Figure 7-9, the precision of the primary peak COG retracker is seen and on the right side, the retracker system using the mean bias removal strategy. For both months, a significant reduction in standard deviation and scattered low precision measurements can be observed throughout the test region. In the west of Novaya Zemyla, a high volatility in standard deviation of PP COG is present in February. According to Figure 4-6, the ice concentration varies significantly in this area, resulting in more complex waveforms. Using the combined retracker with a MBC removal method, there is no clear surface dependent pattern left in the data, as the precision was improved throughout the test region. Furthermore, the reduction of data points in the retracker system becomes apparent.

The dependency of the retracker performance based on the surface type becomes apparent in June. For both the PP COG and the retracker system, a slightly higher standard deviation can be observed around Novaya Zemyla. North of this region, at around 78° latitude a ring of lower standard deviation is observed followed by high standard deviations at northern latitudes. The area around Novaya Zemyla is surrounded by open water, while at higher latitudes the sea ice concentration increases (see Figure 4-6). This relation between the surface type and the precision performance is coherent with the findings in Section 6-1, where it was shown that leads have the highest precision performance compared to open ocean and sea ice. The slightly higher standard deviation remains around Novaya Zemyla for June 2011 also in the retracker system.

In conclusion, the increase in precision performance is the decisive factor for the selection of a bias removal strategy for the Arctic retracker system. Nevertheless, more research into the performance of accuracy needs to be done. However, currently there is no clear solution available for this problem given the extreme conditions in the Arctic.

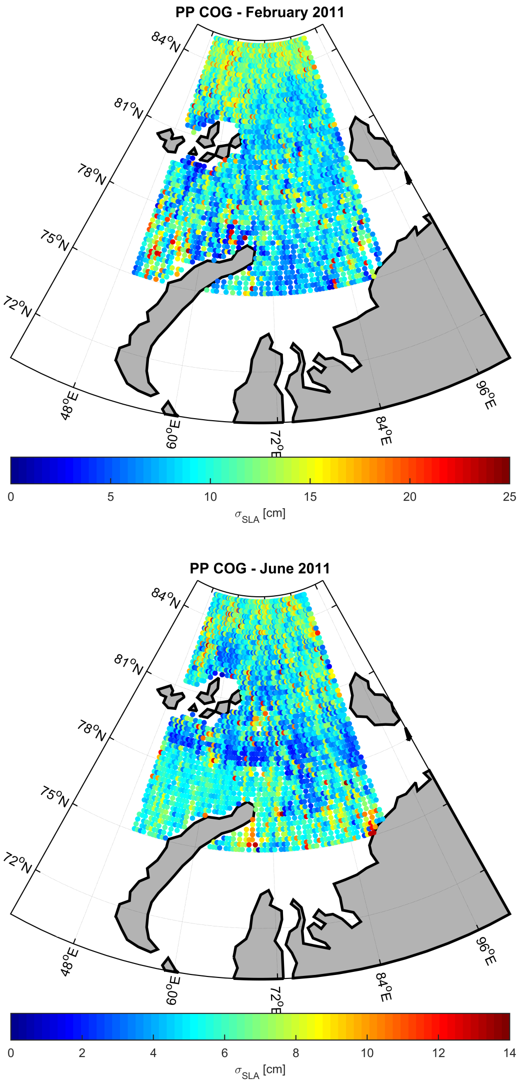

Figure 7-9: The mean standard deviation over the test region for February (top) and June (bottom) 2011. *Left:* The primary peak COG retracker is used. *Right:* The retracker system using a mean bias removal approach with COG as a base retracker.

Chapter 8

Conclusions and Recommendations

As the research focuses on a new approach of a year round retracking system in the Arctic, conclusions and recommendations are presented in order to further improve the implementation of this research.

8-1 Conclusions

The launch of CryoSat-2 in 2010 led to a significant advancement in the field of satellite altimetry. With an on-board Synthetic Aperture Radar (SAR) altimeter and its polar orbit, CryoSat-2 is able to perform frequent, high resolution measurements of the Arctic region. The performance of SAR altimeter varies for different surface types such as water or sea ice.

Given the high seasonality in the Arctic, which leads to a constant change in ocean, ice and sea ice present, it is essential to have a year round retracking system in order to avoid a decrease in measurement performance. The purpose of this Master thesis is as following:

> *The objective of this research is to improve SAR waveform retracking in the Arctic region by analyzing different retrackers on their performance in varying (Arctic) conditions and combine the positive behavior into one retracker system.*

In order to develop a year round retracking system, first the waveforms received by the altimeter need to be classified given their surface terrain. Based on their statistical behavior and number of peaks, waveforms are classified into open ocean, sea ice and leads observations. Leads are waveforms caused by measuring large fractures in sea ice. This results in the presence of water in these up to hundred meter wide and kilometers long cracks.

The waveform classification showed a high seasonality caused by the changing numbers of ocean, leads and sea ice waveforms in a selected test region throughout 2011. From January until April, sea ice is the dominant waveform class, while leads have the highest presence in May to June. Finally, the number of ocean observations is the largest for the rest of the year.

The second part of this research focuses on the retracker performance analysis. In total four retrackers are analyzed, the three empirically based primary peak threshold, primary peak Center of Gravity (COG) retracker and ESA retracker and the physical SAMOSA retracker. While empirical retrackers determine the retracking location based on statistics, the physical retracker takes surface properties into considerations.

The performance of the retrackers is assessed based on their accuracy and their precision per waveform class as discussed in Chapter 6. The accuracy is assessed by an Envisat crossover analysis and three tide gauges in the test region. However, due to uncertainties in the CryoSat's radial offset the value of the crossover analysis is limited. Furthermore, the tide gauges represent one spatial observation in a coastal area and are compared to an entire test region limiting the meaning of the in-situ observations significantly. The reference data is used for a comparison with ocean waveforms, however, accuracy reference data for sea ice or leads is not available.

SAMOSA has a high precision and accuracy performance for ocean waveforms, as its physical fully analytic waveform function can provide a good fit for the predictable ocean waveforms. However, for irregular waveforms, like leads and sea ice, the primary peak retrackers have the highest precision. Since the primary peak retrackers only analyze the peak with the maximum power, they are less prone to noise or multiple smaller peaks compared to full waveform fitting retrackers (like SAMOSA or ESA). The ESA retracker has the lowest precision and accuracy performance for all waveform classes.

A year round retracker system for the Arctic is selected based on the best performance with respect to accuracy and precision for ocean waveforms and precision for leads and sea ice. Precision is the defining parameters for irregular waveforms as there is no reference data available for these waveforms, resulting in no accuracy determination.

To minimize the offset of the year round retracker sytem, five different bias removal strategies are evaluated. The first method is the mean bias method, which computes the offset of two retrackers per track over open ocean as the waveform behavior is predictable. This offset is then consequently applied to other waveform classes as a constant. The second method uses a parabolic dependency of the offset on significant wave height, *SWH*, per waveform class. Two strategies are assessed using the mean bias method with once the primary peak COG retracker as a basis and once SAMOSA. The third strategy uses the significant wave height dependency with primary peak COG as a base retracker. Finally, two hybrid models are applied. The first one corrects the bias of open ocean using *SWH* dependency and for leads and sea ice the mean bias method. The second hybrid model applies the *SWH* bias removal to open ocean and leads, while the offset in sea ice is removed by the mean bias approach.

Due to scarce observations of *SWH* for leads and sea ice, the third strategy proved to include an insufficient number of observations. The SAMOSA based mean bias method, also excluded a large number of data points, as strong prefiltering applied, leaving less data compared to the primary peak retrackers.

Based on precision as well as data set size, it was determined that the year round retracker system using a primary peak COG base mean bias approach performs best with a mean standard deviation of 3.55 cm and a mean improvement with respect to the primary peak COG retracked sea level anomaly of 47.1%.

8-2 Recommendations

This research paved the road to the development of a year round retracking system while analyzing the surface characteristics of the Arctic. In order to further develop this retracker system, some recommendations are discussed in the following.

Baseline C

The quality of the sea level anomaly, strongly depends on the quality of the range measurement and applied corrections. In this research, ESA's Baseline B data was used while compensating for the known time tag bias and range offset. To further improve the quality of the observations, it is recommended to implement Baseline C data in the retracker system as it reduces the uncertainties in the sea level anomaly. The Baseline C product includes a more precise orbit model and improved attitude information by implementing the known biases in roll and pitch angles [28]. During this research, the backwards processing of the data to get Baseline C was not yet available for the year 2011.

Accuracy Evaluation

One significant limitations of this research is the evaluation of retracking accuracy. In order to improve the accuracy determination, a test region should be selected around Svalbard or Novaya Zemlya. Nevertheless, the issue of comparing one spatial observation with an entire test region remains. Thus, these tide gauge data provide a good insight into the accuracy of the data, however, they should not be used as absolute reference.

Another method to determine the accuracy is using HY-2 data. HY-2A (HaiYang-2A) is an altimeter satellite launched by the China National Space Administration (CNSA) focusing on ocean application. It was launched in August 2011 and has a comparable performance as Jason-2 [61]. With an inclination of 99.3° [62], latitudes of up to 80.7° are reached, providing crossover opportunities in the Arctic.

AVISO+ provides access to the data using their ftp server. However, the data provided by AVISO+ does not cover the year 2011, but only starts in April 2014. To improve both the retracker accuracy and the reference accuracy, it is suggested to compute the annual performance of different retrackers starting in April 2014 until April 2015 on a test region including the coast of Svalbard.

Mean Sea Surface

The performance of the sea level anomaly, *SLA*, depends on the accuracy of the mean sea surface that is used as is shown by Eq. (6-1). In this research the mean sea surface model of DTU13 was used. Denmarks Tekniske Universitet (DTU) published an updated version of its mean sea surface called DTU15 in December 2015 [36]. Therefore, it was therefore not available in time for the data processing of this research. The advantage of DTU15 is that it includes CryoSat-2 observations resulting in a reliable high resolution Arctic model [63]. Figure 8-1 shows the difference between the mean sea surface model of DTU15 and DTU13 given a 1 minute resolution. The difference in the test region between DTU15 and DTU13 range from -10 cm to 10 cm and can therefore significantly impact the retracker accuracy.

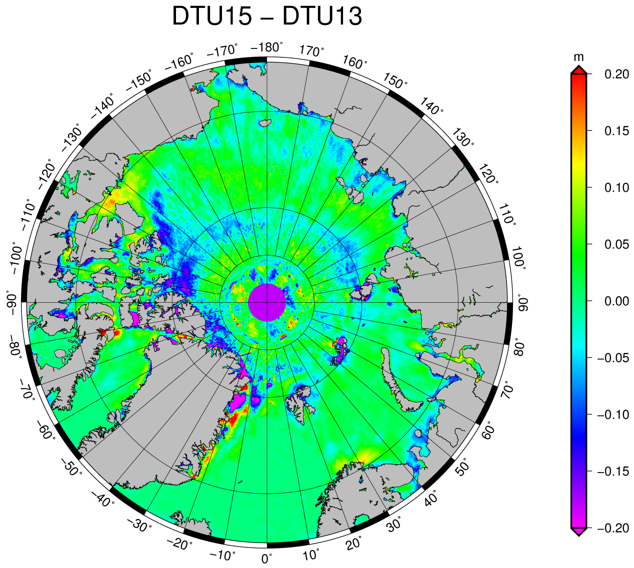

Figure 8-1: The difference in DTU15 and DTU13 mean sea surface for the Arctic at a 1 minute resolution [36].

Radial Offset

The radial offset of CryoSat-2 is well defined for Low-Resolution Mode (LRM) observations, however, a significant uncertainty remains in the radial offset for SAR observations [57]. It is obvious, that the precision of this offset strongly affects the value of a crossover analysis. Therefore, it is suggested to further investigate the range bias of CryoSat-2 in SAR mode. An accurate determination of this offset would also directly influence the accuracy evaluation of the different retrackers and then consequently, the retracker system.

Bias Removal Strategies

One significant limitation of the bias removal strategy was the scarce data of significant wave height and wind speed. In order to further improve the bias removal approach, the significant wave height data as provided by the WaveWatchIII model by National Oceanic and Atmospheric Administration (NOAA) can be used.

However, when using the WaveWatchIII model, the difference between the significant wave height provided by SAMOSA and the one provided by the model should be analyzed, as the NOAA model is based on a numerical approach [64]. In case there is an offset between these two data sets, this should be accounted for.

Another method that could improve the waveform classification and bias removal is the use of a neural network. Essentially, a neural network processes information in order to retrieve trends and patterns that can be used to predict behavior [59]. A neural network has two segments: training and prediction. During the training phase, the network learns different waveform classes and bias removal strategies based on information provided to it. Once the training is finished, the neural network is able to determine the waveform class and to compute the sea level anomaly using different retrackers. In the last step, the neural network will adjust the computed sea level anomaly in order to be coherent with an a priori selected base retracker.

The use of a neural network for waveform classification has shown to be effective for LRM waveforms using Envisat and SARAL data within the framework of ESA's sea level climate change initiative [65]. Furthermore, [59] showed that the use of a neural network was able to perform bias removal in the coastal area, thus waveforms with a lot of noise. However, when comparing the mean bias approach with the neural network over open ocean, only a small difference in performance was found [59]. Nevertheless, for irregular waveforms, such as coastal ones, sea ice or leads, the neural network performed better. Therefore, it is worth to further investigate the application of neural network and see its performance in the retracker system.

Appendix A

Reference Ellipsoid Adjustment

When comparing altimetry data, it is crucial that the same reference ellipsoid is used. While CryoSat-2 measures with respect to WGS84 (Wold Geodetic System), the mean sea surface determined by DTU and the altimetry data from Radar Altimeter Database System (RADS) are using the TOPEX/Poseidon reference ellipsoid. In this research WGS84 is used as a reference and therefore, the mean sea surface and the RADS data are compensated for this offset.

The difference in the reference ellipsoids is due to the radii and flattening coefficients used. Table A-1 shows these parameters for the two reference ellipsoids.

The geometry and parameters of the ellipsoid are shown in Figure A-1. Based on the ellipsoid relation as shown in Eq. (A-1), the radius, R, for a changing latitude, ϕ, can be computed. Spherical coordinates are used as given by Eq. (A-2).

$$\frac{x^2}{a^2} + \frac{y^2}{b^2} = 1 \tag{A-1}$$

$$x = R\cos\phi \qquad y = R\sin\phi \tag{A-2}$$

The radius with respect to the center of the Earth at a given latitude can then be determined by Eq. (A-3). Using the coefficients provided in Table A-1, the radius based on the two reference ellipsoid can be computed. The difference in radii for different latitudes is shown in Figure A-2.

$$R(\phi) = \left(\frac{\cos^2\phi}{a^2} + \frac{\sin^2\phi}{b^2}\right)^{-1/2} \tag{A-3}$$

Table A-1: The parameters describing WGS84 and TOPEX/Poseidon reference ellipsoid.

	WGS84	**TOPEX/Poseidon**
Radius [km]	6378.137	6378.1363
Flattening coefficient [-]	1/298.257223	1/298.257

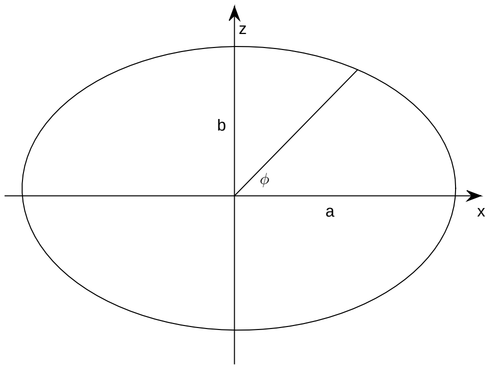

Figure A-1: The geometry of the ellipsoid. The equatorial radius is indicated by A and the polar radius is shown by B. The latitude is given by ϕ.

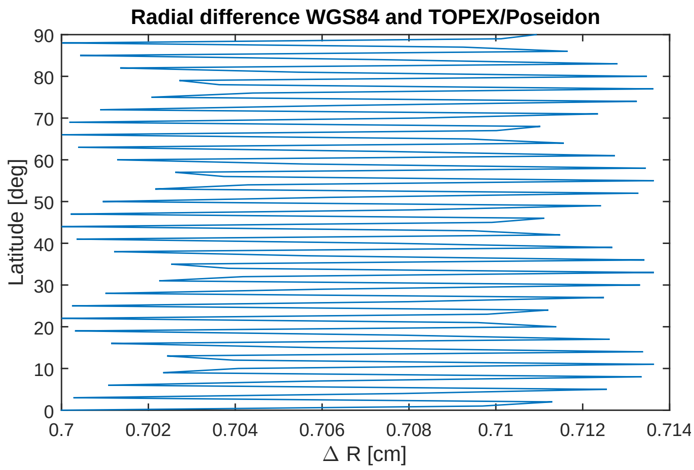

Figure A-2: The difference in WGS84 and TOPEX/Poseidon reference ellipsoid as a function of latitude.

Appendix B

SAMOSA2 Performance

The principle of SAMOSA2 is the same as for SAMOSA3 that is implemented in this research. It is a physical retracker that includes more terms of the Bessel functions with respect to SAMOSA3 [21]. Thus, SAMOSA3 is a simplification of SAMOSA2. The significant difference to SAMOSA3 is that SAMOSA2 is not fully analytic and requires more computation power [58]. By implementing the first order Bessel term, additional parameters of the surface are taken into consideration such as the sea height standard deviation as expressed by Eq. (5-13).

The behavior of the sea level anomaly of SAMOSA2 with respect to SAMOSA3 was discussed in Section 6-3. It was observed that for ocean waveforms the difference in sea level anomaly between these two retrackers is rather small. For irregular waveforms such as leads or sea ice a large deviation occurs both positively and negatively. This behavior is caused since SAMOSA is a physical retracker, thus it is less precise when retracking irregular waveforms compared to empirical retrackers.

Figure B-1 shows the standard deviation of SAMOSA2 for different waveform classes for the November track 2011. The precision performance for ocean waveforms is slightly higher for SAMOSA2 compared to SAMOSA3, leading to the lowest precision of all retrackers. However, for leads, the standard deviation of SAMOSA2 is significantly larger with respect to all retrackers. SAMOSA2 is not able to determine more than one observation for sea ice, due to the filtering criteria. When determining the 1 Hz standard deviation per waveform class, an observation is only considered if at least 5 measurements are used. Thus, observations with less data points in a one second interval are discarded. For unclassified waveforms, SAMOSA2 behaves very closely to SAMOSA3 with only a few points having a significant deviation.

Overall, the inclusion of a higher order Bessel function is beneficial for open ocean observations. However, for more complex waveforms SAMOSA2 fails to provide precise results, leading in a larger deviation with respect to the simplified SAMOSA3 retracker.

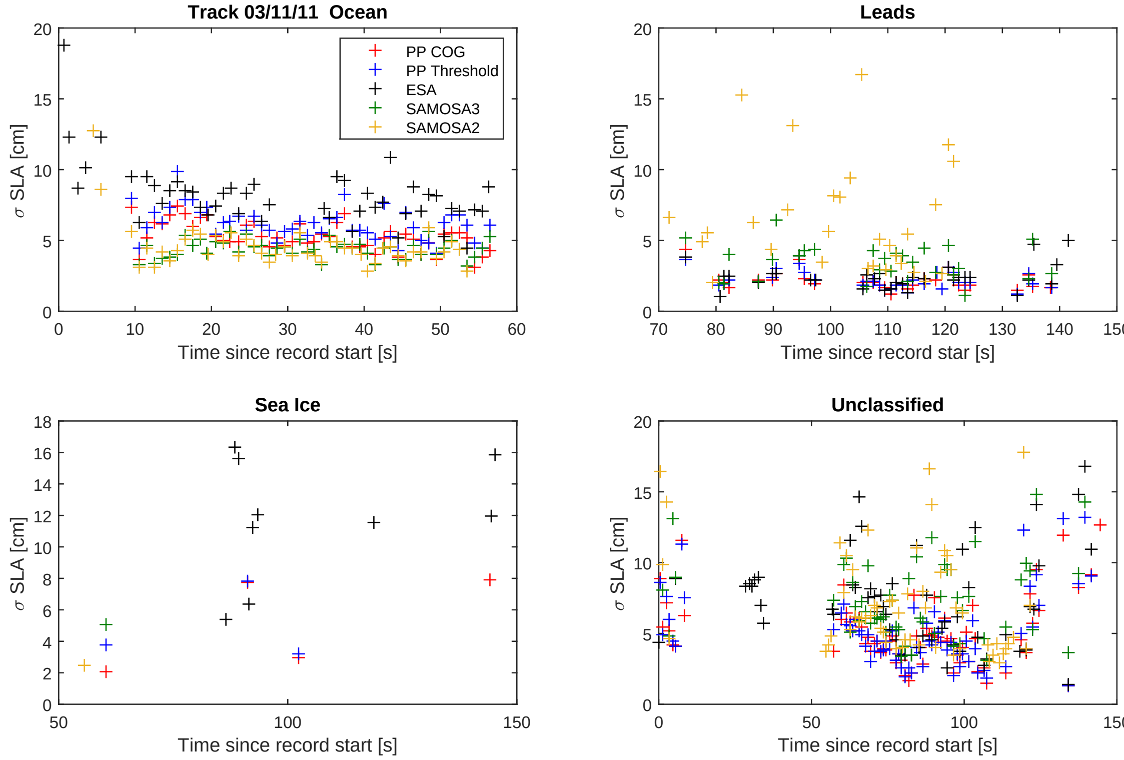

Figure B-1: The standard deviation of SAMOSA2 is compared to SAMOSA3 for the 03/11/2011 track, PP COG, PP threshold and ESA retracker. *Top left:* Ocean waveforms. *Top right:* Lead waveforms. *Bottom left:* Sea ice waveforms. *Bottom right:* Unclassified waveforms.

Bibliography

[1] R. K. Raney, "The delay/doppler radar altimeter," *IEEE Transactions on Geoscience and Remote Sensing*, vol. 36, pp. 1578–1588, September 1998.

[2] N. Kurtz, N. Galin, and M. Studinger, "An improved CryoSat-2 sea ice freeboard retrieval algorithm through the use of waveform fitting," *The Cryosphere Discussions*, vol. 8, pp. 1217–1237, July 2014.

[3] V. Helm, *Airborne SAR/Interferometric Radar Altimeter System (ASIRAS)-Kalibrierung, Validierung und Interpretation der Messergebnisse*. PhD thesis, Universität Bremen, 2008.

[4] M. Jain, O. B. Andersen, J. Dall, and L. Stenseng, "Sea surface height determination in the Arctic using Cryosat-2 SAR data from primary peak empirical retrackers," *Advances in Space Research*, vol. 55, pp. 40–50, 2015.

[5] J. Benveniste, *Coastal Altimetry*, ch. Radar Altimetry: Past, Present and Future, pp. 1–17. Springer, 2011.

[6] ESRIN - ESA and Mullard Space Science Laboratory - University College London, *CryoSat Product Handbook*, April 2010.

[7] B. D. Tapley, B. E. Schutz, and G. H. Born, *Statistical Orbit Determination*. Elsevier Academic Press, 2004.

[8] Mullard Space Science Laboratory - University College London, "L2 siral mode monitoring." `http://cryosat.mssl.ucl.ac.uk/qa/mode.php`. Accessed on 24-05-2015.

[9] P.-Y. Le Traon, "Satellite altimetry." 2nd Advanced Training Course in Ocean Remote Sensing, October 2007.

[10] D. Chelton, J. Ries, B. Haines, L.-L. Fu, and P. Callahan, *Satellite Altimetry and Earth Sciences - A handbook for Techniques and Applications*, ch. Satellite Altimetry, pp. 1–131. Academic Press, 2001.

[11] G. Seeber, *Satellite Geodesy*. de Gruyter, 2nd ed., 2003.

[12] O. Andersen and R. Scharroo, *Coastal Altimetry*, ch. Range and Geophysical Corrections in Coastal Regions: And Implications for Mean Sea Surface Determination, pp. 103–145. Springer, 2011.

[13] D. Wingham, C. Francis, S. Baker, C. Bouzinac, D. Brockley, R. Cullen, P. de Chateau-Thierry, S. Laxon, U. Mallow, C. M. M. Phalippou, G. Ratier, L. Rey, F. Rostan, P. Viau, and D. Wallis, "CryoSat: A mission to determine the fluctuations in the Earth's land and marine ice fields," *Advances in Space Research*, vol. 37, pp. 841–871, 2006.

[14] C. M. Rush, "Ionospheric radio propagation models and predictions - a mini-review," *IEEE Transactions on Antennas and Propagation*, vol. 34, pp. 1163–1170, September 1986.

[15] NASA JPL, "Global ionospheric maps." http://iono.jpl.nasa.gov/gim.html. Accessed on 08-07-2015.

[16] Satellite Oceanographic Consultants, "SAR Altimetry Coastal & Open Ocean Performance." http://satoc.eu/projects/SCOOP/, 2015. Accessed on 15-01-2016.

[17] J. Huang and M. Véronneau, "Canadian gravimetric geoid model 2010," *Journal of geodesy*, vol. 87, no. 8, pp. 771–790, 2013.

[18] S. Dinardo, B. Lucas, and J. Benveniste, "Grid processing on demand." http://gpod.eo.esa.int/, 2015.

[19] D. Cartwright and R. Tayler, "New computations of the tide-generating potential," *Geophysical Journal International*, vol. 23, no. 1, pp. 45–73, 1971.

[20] AVISO+, "Correction of high frequency signals." http://www.aviso.altimetry.fr/en/data/products/auxiliary-products/atmospheric-corrections/description-atmospheric-corrections.html. Accessed on 08-07-2015.

[21] R. K. Raney, "CryoSat SAR-Mode Looks Revisited," *IEEE Geosciene and Remote Sensing Letters*, vol. 9, pp. 393–397, May 2012.

[22] J. B. Campbell, *Introduction to Remote Sensing*. Guilford Publications, 3rd ed., 2002.

[23] G. S. Brown, "The average impulse response of a rough surface and its applications," *IEEE Transactions on antennas and propagation*, vol. 25, pp. 67–74, January 1977.

[24] E. J. Walsh, "Pulse-to-pulse correlation in satellite radar altimeters," *Radio Science*, vol. 17, pp. 786–800, July-August 1982.

[25] R. Francis, "Jason-CS or, Sentinel-6/ Jason-CS." ESA presenation, 2013.

[26] R. K. Raney, "Resolution and Precision of a Delay-Doppler Radar Altimeter," in *OCEANS, 2005. Proceedings of MTS/IEEE*, vol. 3, pp. OCEANS, 2005. Proceedings of MTS/IEEE, 2005.

[27] S. Dinardo, B. Lucas, and J. Benveniste, "SAR Altimetry in Coastal Zone: Performance, Limits, Perspective." 5th Coastal Altimetry Workshop, October 2011.

[28] M. Scagliola, *Main evolutions and expected quality improvement in SAR/SARin Baseline Level1b products]*. ARESYS, October 2014.

[29] L. Stenseng, *Algorithm Theoretical Baseline Document - Polar Ocean*. DTU Space, 0.9 ed., May 2014.

[30] M. Jain, *Improved sea level determination in the Arctic regions through development of tolerant altimetry retracking*. PhD thesis, DTU Space, August 2015.

[31] C. Gommenginger, P. Thibaut, L. Fengolio-Marc, G. Quartly, X. Deng, J. Gómez-Enri, P. Challenor, and Y. Gao, *Coastal Altimetry*, ch. Retracking Altimeter Waveforms Near the Coasts, pp. 61–103. Springer, 2011.

[32] A. Wernecke and L. Kaleschke, "Lead detection in Arctic sea ice from CryoSat-2: quality assessment, lead area fraction and width distribution," *The Cryosphere*, vol. 9, no. 5, pp. 1955–1968, 2015.

[33] M. Scagliola, *Beam Behavior Parameters in CryoSat Level1b products*. aresys, September 2014.

[34] T. W. Armitage and M. W. Davidson, "Using the interferometric capabilities of the ESA Cryosat-2 mission to improve the accuracy of sea ice freeboard retrievals," *Geoscience and Remote Sensing, IEEE Transactions on*, vol. 52, no. 1, pp. 529–536, 2014.

[35] F. M. Dekking, *A Modern Introduction to Probability and Statistics: Understanding why and how*. Springer Science & Business Media, 2005.

[36] DTU Space, "Public server." Accessed on 18-09-2015.

[37] Lotus, *Algorithm Theoretical Baseline Document for SAR mode processing over ocean*, June 2014.

[38] Earth System Research Laboratory - National Oceanic & Atmospheric Adminitration, "Arctic ocean leads." http://www.esrl.noaa.gov/csd/projects/arcpac/photos/leads.php. Accessed on 29-02-2016.

[39] R. Saldo, "Sea ice denmark." http://www.seaice.dk/Nzipfiles/.Archive/. Accessed on 04-11-2015.

[40] C. H. Davis, "A Robust Threshold Retracking Algorithm for Measuring Ice-Sheet Surface Elevation Change from Satellite Radar Altimeters," *IEEE Transactions on Geoscience and Remote Sensing*, vol. 35, pp. 974–979, July 1997.

[41] Satellite Oceanographic Consultants, "SAMOSA." http://www.satoc.eu/projects/samosa/. Accessed on 26-06-2015.

[42] L. Phalippou and V. Enjolras, "Re-tracking of SAR altimeter ocean power-waveforms and related accuracies of the retrieved sea surface height, significant wave height and wind speed," in *Geoscience and Remote Sensing Symposium, 2007. IGARSS 2007. IEEE International*, pp. 3533–3536, IEEE, 2007.

[43] C. Ray, C. Martin-Puig, M. P. Clarizia, S. Dinardo, and C. Gommenginger, "SAR Altimeter Backscattered Waveform Model," *IEEE Transactions on Geoscience and Remote Sensing*, vol. 53, pp. 911–918, February 2015.

[44] S. Dinardo, B. Lucas, and J. Benveniste, “The Sentinel-3 SAMOSA Model and Retracking.” SAR Altimetry Training Course, October 2014.

[45] M. Jain, C. Martin-Puig, O. Andersen, L. Stenseng, and J. Dall, “Evaluation of SAMOSA3 adapted retracker using CryoSat-2 SAR altimetry data over the Arctic ocean,” in *Geoscience and Remote Sensing Symposium (IGARSS), 2914 IEEE International*, pp. 5115–5118, July 2014.

[46] J. Benesty, J. Chen, Y. Huang, and I. Cohen, *Noise Reduction in Speech Processing*. Springer, 2009.

[47] C. Dufau, C. Martin-Puig, and L. Moreno, *Coastal Altimetry*, ch. User Requirements in the Coastal Ocean for Satellite Altimetry, pp. 51–60. Springer, 2011.

[48] R. Raney, “Advances in Oceanic Radar Altimetry: CryoSat and Beyond.” SAR Altimetry Training Course, October 2014.

[49] K. O. Emery and D. G. Aubrey, *Sea levels, land levels, and tide gauges*. Springer Science & Business Media, 2012.

[50] Permanent Service for Mean Sea Level, “Tide gauge data,” 2015. Accessed on 08-12-2015.

[51] G. A. Milne, “Glacial isostatic adjustment,” *Handbook of Sea-Level Research*, pp. 419–437, 2015.

[52] O. Henry, P. Prandi, W. Llovel, A. Cazenave, S. Jevrejeva, D. Stammer, B. Meyssignac, and N. Koldunov, “Tide gauge-based sea level variations since 1950 along the Norwegian and Russian coasts of the Arctic Ocean: Contribution of the steric and mass components,” *Journal of Geophysical Research: Oceans*, vol. 117, no. C6, 2012.

[53] O. Andersen, P. Knudsen, and L. Stenseng, *The DTU13 MSS (Mean Sea Surface) and MDT (Mean Dynamic Topography) from 20 years of satellite altimetry*. Springer, 2015.

[54] S. Pinori, D. Cotton, J. Louis, M. Talone, and P. Femenias, “Envisat altimeter system: Near real time long-term monitoring,” in *Geoscience and Remote Sensing Symposium (IGARSS), 2012 IEEE International*, pp. 2665–2668, IEEE, 2012.

[55] DEOS and NOAA, “Radar altimeter database system.” http://rads.tudelft.nl/rads/rads.shtml. Accessed on 14-12-2015.

[56] B. Soussi, *ENVISAT Altimeter Level 2 User Manual*. CLS, 1.4 ed., October 2011.

[57] D. Dettmering and W. Bosch, “Performance of ESA CryoSat-2 GDR data over open ocean,” in *Proceedings of CryoSat Third User Workshop. Ouwehand, L.(ed.), Dresden, Germany*, 2014.

[58] C. Gommenginger, C. Martin-Puig, S. Dinardo, D. Cotton, M. Srokosz, and J. Benveniste, “Improved altimetric accuracy of SAR altimeters over the ocean: Observational evidence from Cryosat-2 SAR and Jason-2,” *Proc. OSTST Meet*, pp. 19–21, 2011.

[59] N. H. Idris, *Development of new retracing method for mapping sea level over the shelf areas from satellite altimeter data*. PhD thesis, The University of Newcastle Australia, September 2014.

[60] R. K. Pearson, *Mining imperfect data: Dealing with contamination and incomplete records*. Siam, 2005.

[61] CLS, *SSALTO/DUACS User Handbook: (M)SLA and M(ADT) Near-Real Time and Delayed Time Products*, 4.4 ed., June 2015.

[62] AVISO+, "Hy-2." http://www.aviso.altimetry.fr/?id=593&L=0, 2016. Accessed on 22-02-2016.

[63] G. Piccioni, O. Andersen, and L. Stenseng, "SAR altimetry for Mean Sea Surface determination in the Arctic," in *S3 for Science*, 2015.

[64] H. Tolman, "User manual and system ocument of WAVEWATCHIII," Tech. Rep. Version 4.18, Environmental Modeling Center, March 2014.

[65] P. Thibaut, J.-C. Poisson, D. Hoang, G. Quartly, and A. Kurekin, "Improving Sea Level record in Arctic using Envisat Altimeter Measurements," in *EGU General Assembly Conference Abstracts*, vol. 17, p. 11948, 2015.